

A SEMI-SUPERVISED LEARNING METHOD FOR THE IDENTIFICATION OF BAD EXPOSURES IN LARGE IMAGING SURVEYS

YUFENG LUO^{1,2,3,*}, ADAM D. MYERS¹, ALEX DRLICA-WAGNER^{4,5,6,7}, DARIO DEMATTIES³, SALMA BORCHANI¹,
FRANK VALDES⁸, ARJUN DEY⁸, DAVID SCHLEGEL⁹, RONGPU ZHOU⁹, AND DESI LEGACY IMAGING SURVEYS TEAM

¹Department of Physics and Astronomy, University of Wyoming, 1000 E. University Ave., Laramie, WY 82071, USA

²School of Computing, University of Wyoming, 1000 E. University Ave., Laramie, WY 82071, USA

³Mathematics and Computer Science Division, Argonne National Laboratory, Lemont, IL

⁴Fermi National Accelerator Laboratory, P.O. Box 500, Batavia, IL 60510, USA

⁵Department of Astronomy and Astrophysics, University of Chicago, Chicago, IL 60637, USA

⁶Kavli Institute for Cosmological Physics, University of Chicago, Chicago, IL 60637, USA

⁷NSF-Simons AI Institute for the Sky (SkAI), 172 E. Chestnut St., Chicago, IL 60611, USA

⁸NSF NOIRLab, 950 N Cherry Ave, Tucson, AZ 85719, USA and

⁹Lawrence Berkeley National Laboratory, 1 Cyclotron Road, Berkeley, CA 94720, USA

Version July 18, 2025

ABSTRACT

As the data volume of astronomical imaging surveys rapidly increases, traditional methods for image anomaly detection, such as visual inspection by human experts, are becoming impractical. We introduce a machine-learning-based approach to detect poor-quality exposures in large imaging surveys, with a focus on the DECam Legacy Survey (DECaLS) in regions of low extinction (i.e., $E(B - V) < 0.04$). Our semi-supervised pipeline integrates a vision transformer (ViT), trained via self-supervised learning (SSL), with a k-Nearest Neighbor (kNN) classifier. We train and validate our pipeline using a small set of labeled exposures observed by surveys with the Dark Energy Camera (DECam). A clustering-space analysis of where our pipeline places images labeled in “good” and “bad” categories suggests that our approach can efficiently and accurately determine the quality of exposures. Applied to new imaging being reduced for DECaLS Data Release 11, our pipeline identifies 780 problematic exposures, which we subsequently verify through visual inspection. Being highly efficient and adaptable, our method offers a scalable solution for quality control in other large imaging surveys.

1. INTRODUCTION

The Astro2020 decadal survey (National Academies of Sciences, Engineering, and Medicine 2023) highlighted the increasing importance of advanced pipelines for processing data from large astronomical surveys, and how scientific results will crucially depend on these pipelines. Identifying bad exposures is a key step in any pipeline to optimize the quality of images from sky surveys. However, this step can often be laborious. Traditionally, the bad exposures can be labeled in two ways. First, the observers at the telescope can record the exposure condition and quality during observation. Some issues, such as shaking due to strong winds, can be noted. Further, some common issues, such as hot pixels and cosmic rays, can be detected and fixed using algorithms and available software (van Dokkum 2001; Astropy Collaboration et al. 2022). Some other issues, like seeing and Point Spread Function (PSF) variations, are usually detectable during photometric reductions (Lang et al. 2016). Beyond this, more specific problems, such as ghosting and scattered light, have been historically difficult to handle and have often required special algorithmic treatment. Although some solutions to these problems exist (Patterson & Wells 2003; Kent 2013), they are usually built for a specific telescope or camera. In this case, astronomers have to visually inspect exposures to determine which might be problematic and/or evaluate the image quality during the overall data reduction process. Astronomers often also have to explicitly construct separate models or metrics to study each problematic imaging systematic.

As larger surveys proceed to everyday operations, the number of exposures in their associated imaging campaigns is likely to become too high for a human expert to visually inspect every image. Further, as the number of pixels achieved by cameras increases, features in images are likely to become more complex, which will make the identification of bad exposures even more taxing. As an example, the LSSTCam on the Vera C. Rubin telescope utilizes a 3.2-gigapixel CCD detector and can observe 10,000 square degrees of sky in a single filter every three clear nights (Ivezić et al. 2019). Despite the increase in scope and complexity of future imaging surveys, the quality of exposures in large campaigns will remain essential to downstream tasks, such as astrometric (e.g., Lang et al. 2009), and photometric (e.g., Stubbs & Tonry 2006) measurements, and target selection to facilitate follow-up studies (e.g., Myers et al. 2023). The bottom line is that unintentionally including bad exposures in the datasets produced by imaging surveys will always be detrimental

*Corresponding author: yluo4@uwyo.edu

to downstream scientific results. Therefore, understanding and identifying problematic exposures will be a difficult but crucial element of next-generation imaging surveys.

While large astronomical surveys have been expanding in volume and quality, more efficient data processing and analysis algorithms have already started to become desirable to take the burden off human inspectors. For example, Zhang & Bloom (2020) and Chang et al. (2021) used Convolutional Neural Networks (CNNs) to, respectively, identify cosmic rays in Hubble Space Telescope images, and detect ghosts and scattered light in Dark Energy Survey (DES) images; Tanoglidis et al. (2021) applied a method based on a Mask Region-Based Convolutional Neural Network (R-CNN) to predict the location of ghosts and scattered light in Dark Energy Camera (henceforth DECam; Flaugher et al. 2015) exposures; and Parisot et al. (2023) applied existing image quality assessment (IQA) algorithms developed for general computer vision applications to score images drawn from the Dark Energy Spectroscopic Instrument (DESI) Legacy Imaging Surveys (dubbed LS in the following text; Dey et al. 2019), based on a predefined set of bad images.

In this work, we focus on using recently developed machine learning (henceforth ML) algorithms to identify bad exposures from DECam. This is a complex problem as each DECam exposure comprises 62 individual CCDs (or 61 CCDs with N30 masked out¹), and problems can be present both on large scales (i.e., the entire exposure) and small scales (i.e., individual CCDs, or even groups of pixels). Some issues with the DECam exposures have been mitigated by the DECam Community Pipeline (CP; Valdes et al. 2014), which is a data reduction pipeline that processes DECam images and produces calibrated images and catalogs. However, some issues, such as ghosting and scattered light, are not fully addressed by the CP, and thus require further investigation. To address this complexity, our pipeline adopts an ML approach based on a Vision Transformer (ViT; Dosovitskiy et al. 2021). ViT is a deep learning model based on the transformer architecture (Vaswani et al. 2017) to capture complex patterns in images, often outperforming traditional convolutional neural networks (CNNs) when trained on large datasets. In particular, we use a pretrained existing ViT in the context of version 2 of the self-Distillation with No Labels (DINOv2) framework (Caron et al. 2021; Oquab et al. 2023). The original ViT was trained with ImageNet (Deng et al. 2009), and we apply that trained ViT to generate representations of an image, generally referred to as a vector “*embedding*.” An embedding is essentially a representation of the features of an image in a high-dimensional parameter space. We then use a k-Nearest Neighbor (kNN) algorithm to classify these embeddings after dimension reduction, and assign categories to images based on a labeled training set.

We aim to simultaneously detect multiple potential problems in an exposure, and use a pipeline that only requires a relatively small training and testing dataset, typically comprising less than 5% of the whole exposure dataset. As a purely data-driven method, our model can be adapted to other telescopes, although we choose to train our model using a dataset from DECam. Our pipeline is also relatively *fast* for inference. To tackle the large volume of data, our framework uses Graphics Processing Units (GPU). GPUs are a highly adaptable and efficient hardware for big datasets and are widely used in ML fields (Steinkraus et al. 2005). Moreover, we take advantage of multi-GPU parallel processing to achieve higher inference speed as long as the model can be fitted into each single GPU.

This paper is organized as follows: Section 2 outlines the dataset we utilize, including the source and volume of the exposures, and the labels associated with some of the exposures. In Section 3, we discuss the details of our pipeline, the use of ViT and the layout of the classification task. We also discuss the training and validation procedure used by our pipeline. In Section 4 we analyze the clustering and classification results from our model. We interpret our results, and compare our model with existing pipelines in Section 5. Finally, we discuss limitations of our current framework and suggest future improvements in Sections 5 and 6.

2. DATASET

The exposures in our dataset are mostly drawn from the LS Data Releases 9, 10, and 11 which we henceforth refer to as DR9, DR10 and DR11. The LS comprise three surveys: the Beijing-Arizona Sky Survey (BASS; Zou et al. 2017), Mayall z-band Legacy Survey (MzLS), and DECam Legacy Survey (DECaLS; Dey et al. 2019).² We focus our analysis on DECam images from DECaLS collected with the Victor M. Blanco 4-meter Telescope³ at the Cerro Tololo Inter-American Observatory (CTIO) in Chile. DR11 also includes exposures from the DECam Local Volume Exploration Survey (DELVE; Drlica-Wagner et al. 2021, 2022), which are incorporated in our dataset. All of the images we consider in this paper are inputs to, or have been reduced by, the DECam Community Pipeline (CP; Valdes et al. 2014, see Section 2.4). A small fraction of the exposures are labeled by experts as problematic across a range of different categories. These labels come from three major sources: the DECam bad exposure list (see Section 2.1), previous experts’ visual inspection labels from DELVE, and a wider list of inspections flagged for the DES (Section 2.2 and Appendix A). In addition, we use bad exposure flags developed for DR9 and DR10 to narrow down the selection of good exposures (see Section 2.3). The numbers of categories that can be used as labels, and the numbers of bad exposures provided by each source are listed in Table 1. There are 256,701 exposures in DR9 and DR10, and 18,315 exposures are labeled with at least 1 CCD image as bad by human experts, which is about 7% of the total exposures.

Exposures from DR9 and DR10 are used in our training and testing process. New exposures that will be added for DR11, as well as old exposures from DR9 and DR10 that are reprocessed for DR11, are included in our inference dataset. Our task is to identify bad exposures from the unlabeled exposures based on the labeled exposures, which is a problem that is well-suited to a multi-class classification-task design. With this problem design, a balanced dataset is essential in the training and evaluation process for the classification. We therefore divide our dataset into three

¹ More details can be found at: <https://noirlab.edu/science/programs/ctio/instruments/Dark-Energy-Camera/Status-DECam-CCDs>

² We use LS to refer specifically to the DECaLS portion of the LS in the following text.

³ <https://noirlab.edu/public/programs/ctio/victor-blanco-4m-telescope/>

exclusive samples:

- A training dataset based on 70% of the labeled exposures and an equal amount of unlabeled good exposures. A 3-fold cross-validation (CV; [Stone 1974](#)) was used in the training.
- A testing dataset based on 30% of the labeled exposures and an equal amount of unlabeled good exposures.
- An inference dataset that includes all exposures that are unlabeled excluding exposures used in the training and testing process.

Source	Number of reported bad exposures	Number of categories
DECam bad exposure list	3014	7
DES list	6667	61
DELVE list	8634	37
LS pipeline (see §2.3) flag	119462	19

TABLE 1. THE NUMBER OF BAD EXPOSURES AND CATEGORIES FROM EACH SOURCE. THE DES AND DELVE SAMPLES ARE SIMILAR, EXCEPT THAT DES INCLUDES ADDITIONAL “NICHE” CATEGORIES.

To balance the training, we added another 10,000 “good” exposures that are not included in any of the three samples listed above, although it is certainly possible that a small, but unknown, fraction of these “good” images include some exposures that have significant issues. [Rolnick et al. \(2018\)](#) has shown that ML algorithms can be robust in classification tasks where a small fraction of label noise (i.e., mislabeled data) exists.

2.1. DECaLS Bad Exposure List

The DECaLS bad exposure list records 3,014 bad exposures identified during DECaLS observations and recorded in an observing log file named `bad_expid.txt`⁴. The issues recorded in the log file can be divided into three major categories: exposure quality, observing conditions, and instrument issues. The log file uses three main flags, which are “possibly saturated” (denoted as 1 in `bad_expid.txt`), “seeing” (denoted as 2), and “other sources” (denoted as 3). We used the first two flags directly to indicate bad exposures. These issues span a large domain and each exposure may have slightly different severity. Therefore, to clearly define the bad exposures in this list, we consider exposures in the list satisfying **any** of the following conditions as bad:

- the exposure flag is set to 1 or 2
- the exposure flag is set to 3, and either one of the conditions:
 - *expfactor* is included in the comment and is less than 1. *expfactor* means the exposure factor of an exposure, and it is used to indicate the amount of light
 - the comment contains one of the keywords: *telescope moving*, *tracking*, *PSF*, *focus*.

The “other source” flag usually has associated comments, which we parsed to capture keywords consistent with the above categories. We expect that seeing, transparency, and telescope instability will influence scales across an entire exposure, whereas other categories may be limited to smaller scales that are more consistent with a single CCD.

Throughout the rest of this paper, we will refer to this list of bad exposures as “the DECaLS Bad Exposure List” or simply “the DECaLS list.”

2.2. Expert-Labeled Exposures

The expert labels we use are provided by astronomers who visually inspected the exposures and evaluated their quality, in particular in the context of DELVE and DES. The aim of DES ([DES Collaboration 2016](#)) is to survey 5000 deg² of the southern sky in five optical bands (*grizY*). The DES expert-labeled bad exposure list is based on the DES Year 6 (Y6) data release. There are 122,531 CCD images labeled as bad from 6,667 exposures. These exposures are categorized into 61 different types of comments. Some of the comments are associated with the same imaging patterns but using different expressions or for different reasons, such as “telescope moving” and “telescope tracking failure.” We therefore combined some cases. Ultimately, we picked the top 10 most frequent issues as our bad exposure labels.

DELVE uses DECam to study ultra-faint galaxies around the Milky Way, Magellanic Clouds, and isolated dwarf galaxies in the Local Volume ([Drlica-Wagner et al. 2021](#)). The expert-labeled bad exposures we use in this paper were assembled on 2023 July 25 as an input into DELVE DR3 ([Tan et al. 2025](#)). The expert-labeled DELVE bad exposure dataset contains 51,445 problematic CCD images from 8,634 exposures. There are 37 bad categories associated with these exposures, and we picked the top 10 most frequent issues, similar to the process we used for the DES dataset.

The bad categories in DES do not perfectly match with the categories in DELVE, so we created a unified list of bad categories to combine identified CCD images from the two lists. The final number of images is shown in Table 2. These two datasets provide a large number of labeled bad exposures, which is an essential prerequisite for effectively training the classifier we use in this paper.

Throughout the rest of this paper, we will refer to the Expert-Labeled Exposures List as “the human expert list” or the list “labeled by human experts.”

⁴ https://github.com/legacysurvey/legacypipe/blob/DR10.2/py/legacyzpts/data/decam-bad_expid.txt

2.3. legacypipe additional flags

legacypipe⁵ is a pipeline based on the **Tractor** (Lang et al. 2016) that is used to process the LS imaging data. As part of the reduction process, **legacypipe** provides a set of flags to indicate the quality of each exposure (see, e.g. Dey et al. 2019, for more information). The quality flags are stored in the survey CCD FITS file as bitmasks ranging from 0 to 18, corresponding to 19 different potential issues.⁶

We used the **legacypipe** flags to remove exposures in the good exposure candidate sets that are not in the DECaLS list nor labeled by human experts. This rejection process will minimize the contamination of the good exposure set by bad exposures, hopefully producing a more accurate training process.

2.4. Community Pipeline

The DECam Community Pipeline (CP; Valdes et al. 2014) is an imaging reduction pipeline that is used to process the DECaLS. The DECaLS images are processed by various CP versions, each of which targets some specific problem and, generally, a later CP version is more comprehensive and thus better than a previous one. The range of CP versions used in the LS is from V4.10 through V5.5LS, with all processing performed later than 2019-06-06.⁷ For each exposure, the CP produces many reduced data files and diagnostics. We chose to use the *ooi* images⁸ produced by the CP for our training process because those images are used for stacking and generating the bricks used for LS processing and better match the large-scale background — they are therefore more representative of the eventual images used for scientific analyses. Some exposures do not have associated *ooi* files because the CP processing ended prematurely due to problems in the exposures. Since those exposure issues are usually very obvious, we ignored them during our training as they did not provide additional useful information.

2.5. Extinction Cut

Because the original Key Projects of the DESI experiment (DESI Collaboration et al. 2016), for which the LS was produced, focused on mainly extragalactic sources, the imaging catalog used for targeting also prioritizes sky areas with lower Galactic extinction to minimize the effect of dust attenuation. High-extinction exposures usually have dust emission features that will interfere with the training of our ML model, because the dust emission in the exposures generates additional (unwanted) features. Therefore, to minimize the influence of Galactic dust, we applied an extinction cut to exclude regions where $E(B - V) \geq 0.04$ (Schlegel et al. 1998), further down-selecting exposures for training.

2.6. Categories of Bad Exposures

As noted in Section 2.2, we choose to reduce our dataset to the 11 categories of bad exposures that are most common and we find can best generalize typical problems. The *Saturated* category only appears in the DECaLS list, while the other 10 categories appear in both the human expert list and the DECaLS list. Each of the categories corresponds to a specific issue for the images, and is drawn from the source list noted in Table 2. We provide a brief synopsis of each category below:

- *Saturated*: This corresponds to a near-saturated exposure (generally taken near to twilight). The labeled data in this category is from the DECaLS list where the exposure flag is set to 1.
- *Clouds.Transparency*: Cloud or humidity issues that affect the transparency during an exposure. The data is from the DECaLS list where the exposure flag is 2 or the comment contains either the keyword *transparency* or *clouds*.
- *PSF*: The Point Spread Function issue. These sorts of issues can also typically be detected by standard (non-ML) photometry pipelines.
- *non-optimal exposure*: The exposure is underexposed or some similar exposure-related issue. This data is from the DECaLS list, where the keyword **expfactor** is included in a comment and is *much* less than 1.
- *Ghost/Scatter*: Ghosting or scattered light is present in an image. We follow the convention of the DES bad exposure list to combine these two effects into one category. These effects are usually caused by very bright sources within or near a given field.
- *NObjects*: This label is provided by the DES Data Management processing pipeline (Morganson et al. 2018). The category indicates that an anomalously large number of sources were detected in the image. This effect may be caused by issues with excess noise or difficulty in sky background estimation.
- *Bad CCD*: The CCD image has no data or has an amplifier issue or has a hot spot (i.e., pixel-level defects).
- *Noise*: The CCD includes some uncharacteristic electronic noise.

⁵ code available at <https://github.com/legacysurvey/legacypipe>

⁶ e.g., <https://www.legacysurvey.org/dri0/bitmasks/#ccd-cuts>

⁷ Information on CP versions: <https://desi.lbl.gov/trac/wiki/DecamLegacy/CPVersions>

⁸ For a more detailed description see <https://noirlab.edu/science/index.php/data-services/data-reduction-software/csd-c-mso-pipelines/pl206#tab10>

- *Wonky*: This category includes problems in exposures with patterns that do not belong to any other category and can be caused by miscellaneous reasons.
- *Telescope moving / tracking failure*: The telescope tracking failed or the telescope unexpectedly moved.
- *Out of focus*: The exposure was out of focus.

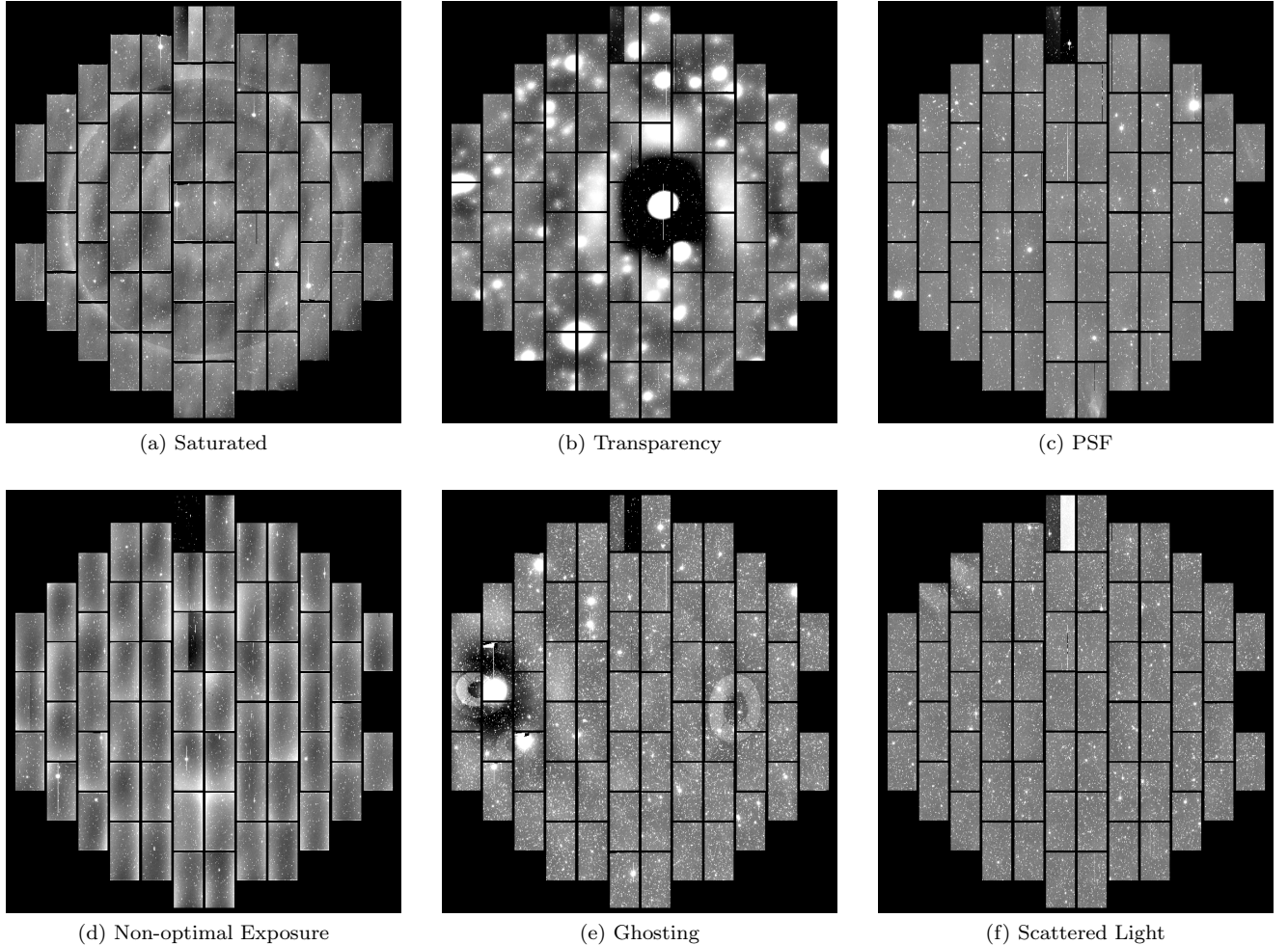


FIG. 1.— A set of representative bad exposures in each category. These examples highlight why some common issues, like *PSF* and *NObjects* can be hard for visual inspectors to detect. Note that some of the exposures have been scaled to highlight the relevant feature. These sorts of scalings are frequently applied and might affect human experts’ judgment, whereas the pipeline we describe in this paper uses raw exposures without any additional processing. It is worth noting that the saturated exposure displays a pattern similar to a flat fielding issue. This is because saturated exposures are mostly taken near twilight when the sky background flux-level will be very high. Therefore, the circular pattern that is visible in a saturated image typically corresponds to the instrument response after the flat-field correction.

2.7. Balancing the Dataset

The kNN training described in Section 3.3 requires a relatively balanced number of images in each category for a good predictive performance. The original labeled dataset is very imbalanced with the ratio of the number of images in the most populated (*Clouds.transparency*) and least populated (*Wonky*) categories being 35. To remedy the imbalance, we downsampled the three categories with the highest number of images and subsequently upsampled the weight of those three categories in the kNN training. Specifically, we downsampled *Clouds.transparency* to one-third of its original size (and correspondingly upweighted the category by 3), downsampled *Ghost.Scatter* by half, and downsampled *NObjects* by 0.75 (increasing the weight by 1.333). With this downsampling and upweighting procedure, the ratio of imbalances between images reduces to 11.8, almost 3-times lower than the original ratio. The comparison between the original and balanced datasets is shown in Figure 3.

2.8. Final Training and Testing Samples

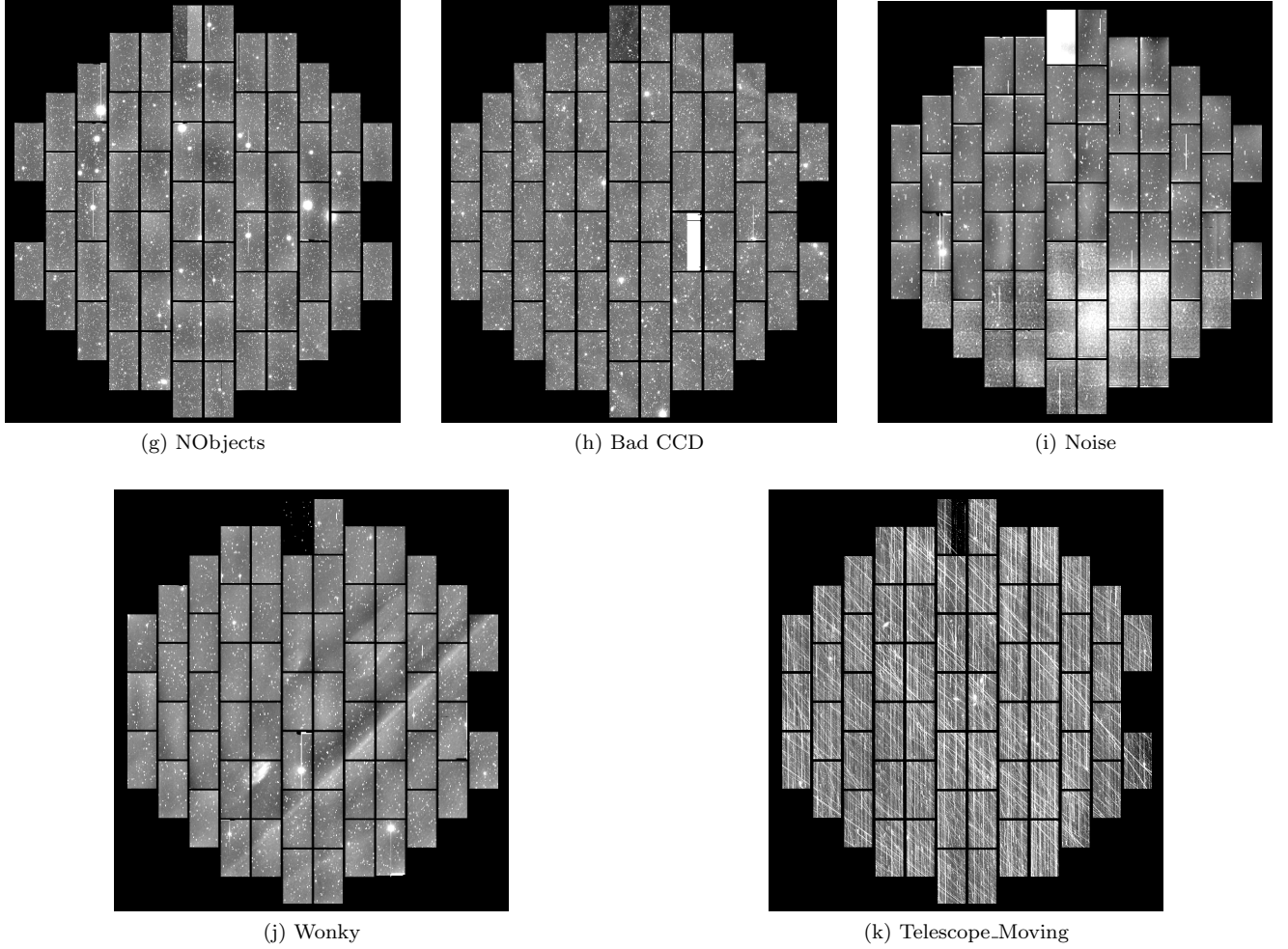


FIG. 2.— Continuation of Figure 1. This figure shows example exposures in the other 5 categories.

Bad Category	DECaLS list	DES + DELVE	from both	Total
<i>saturated</i>	778	0	0	778
<i>clouds or bad transparency</i>	992	22331	15	23338
<i>psf</i>	2359	4781	501	7641
<i>non-optimal exposure</i>	3194	0	0	3194
<i>Ghost/Scatter</i>	0	15755	1	15756
<i>NObjects</i>	0	10093	0	10093
<i>Bad CCD</i>	0	2621	2	2623
<i>Noise</i>	0	2406	61	2467
<i>Wonky</i>	0	667	0	667
<i>Telescope Moving</i>	725	1403	601	2729
<i>out of focus</i>	2160	0	180	2340
Total	10208	60057	1361	73990

TABLE 2. THE CATEGORIES OF THE LABELED BAD EXPOSURES WITH THE NUMBER OF CCD IMAGES IN EACH CATEGORY FROM EACH DATASET SOURCE. “DECALS LIST” AND “DES+DELVE” COLUMNS LIST DATA ONLY FROM THAT SOURCE OF EXPOSURES, EXCLUSIVELY. THE “FROM BOTH” COLUMN LISTS THE EXPOSURES THAT ARE IDENTIFIED IN BOTH LISTS. AS DISCUSSED IN SECTION 2.1 AND 2.2, NOT ALL CATEGORIES ARE PRESENT IN BOTH LISTS.

The final training and testing dataset contains two parts: the combined bad exposure list and the sample of good exposures. The final bad image list combines the DECam bad exposure list and the human-expert list from DES and DELVE. The total number of labeled bad exposures is 73,990, and detailed numbers from each source in each category are shown in Table 2.

As described in Section 2.3, good exposure candidates are all exposures not identified in the combined bad image set or flagged by `legacypipe`. We selected 10,000 good exposures from the candidate set to balance the training dataset, and the final number of training exposures is 40,181.

3. METHOD

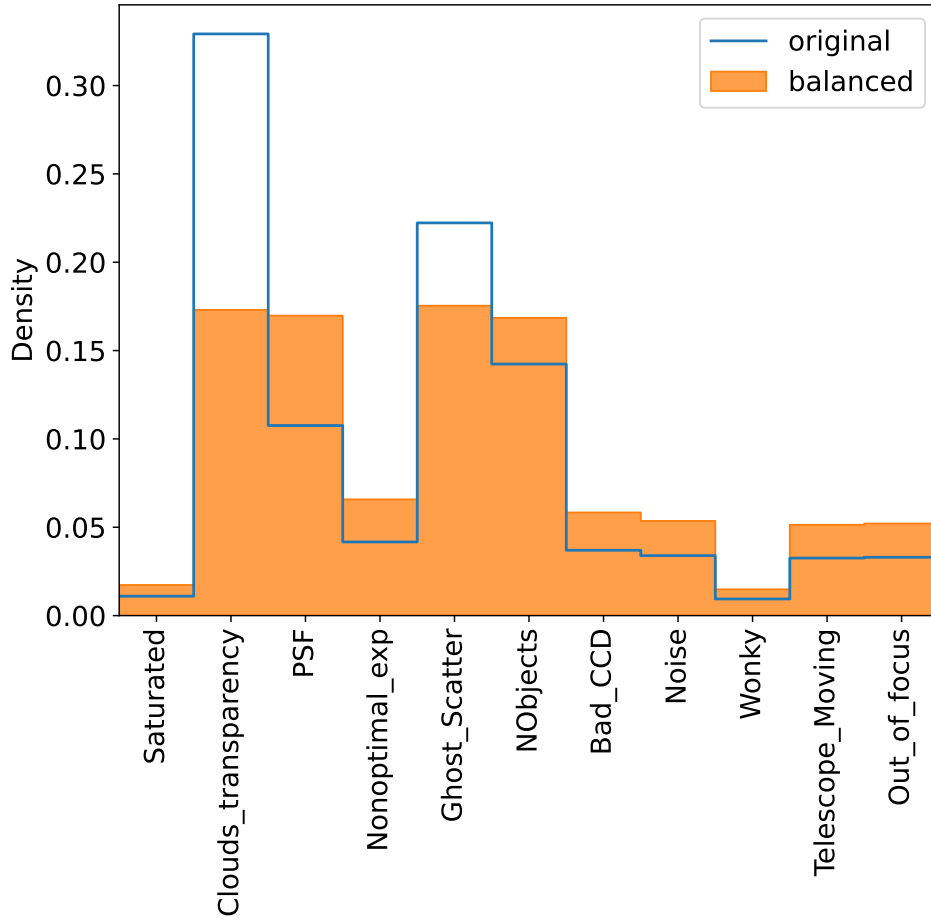


FIG. 3.— The comparison between the original sample of images and the balanced dataset in each category. The “Density” depicts the normalized count of images.

The semi-supervised approach means that our pipeline employs both supervised and unsupervised learning. The two main components in our pipeline are a Deep Neural Network (DNN) trained via Self-Supervised Learning (SSL) (Balestriero et al. 2023; Gui et al. 2024) for pattern recognition and embedding generation, and a classifier for categorizing the images based on the generated embeddings, trained using supervised learning with labels.

SSL demonstrates remarkable potential for uncovering subtle, previously unknown features within data, as well as for removing human subjectivity from the labeling process. These qualities may be valuable when identifying bad exposures, as human experts often merge or confuse similar categories of problems (cf. Section 2.2 where we discuss collapsing 61 different categories down to 10), or entirely miss important features. SSL is also scalable, which should be useful as astronomical surveys continue to grow in size and complexity.

Perhaps most importantly, SSL offers the potential for adaptation because it facilitates easier retraining compared to supervised methods, as it doesn’t require manual labeling of new data. For example, a SSL model trained on current data could be periodically fine-tuned on more recent observations. This process could help the model adapt to subtle changes in image characteristics or new types of artifacts, all without requiring manual annotation of these new examples.

Given the benefits of SSL, our pipeline is built around a pretrained Vision Transformer (ViT) model (Dosovitskiy et al. 2021), a powerful deep learning architecture that has shown impressive performance on a wide range of computer vision tasks (e.g., Kirillov et al. 2023; Azad et al. 2024). Our pipeline comprises three sections: a Deep Neural Network – ViT – for pattern recognition and embedding generation, an embedding post-processor, and a classifier. The input to the pipeline is a single CCD image and the output is a vector of probabilities associated with each issue category for the image. The pipeline is tuned using Hyperparameter Optimization (HPO) to improve the prediction performance (e.g., Franceschi et al. 2024).

As each exposure comprises 61 or 62 CCD images as noted in Section 1, running each image through our pipeline is computationally demanding for both the training and inference stages of our classification process. Further, some features, such as transparency issues due to cloud, or unexpected movement of the entire telescope due to, e.g., wind shake, are large-scale and can affect multiple CCD images. This means that we have to design our model to balance efficiency and accuracy. Therefore, for exposure-level information, we randomly draw 20 CCD images from each exposure and employ a “voting consensus” method. Basically, if 10 of the 20 CCDs are considered bad, then the entire exposure will be labeled as bad. We will discuss the details of the pipeline in the rest of this section.

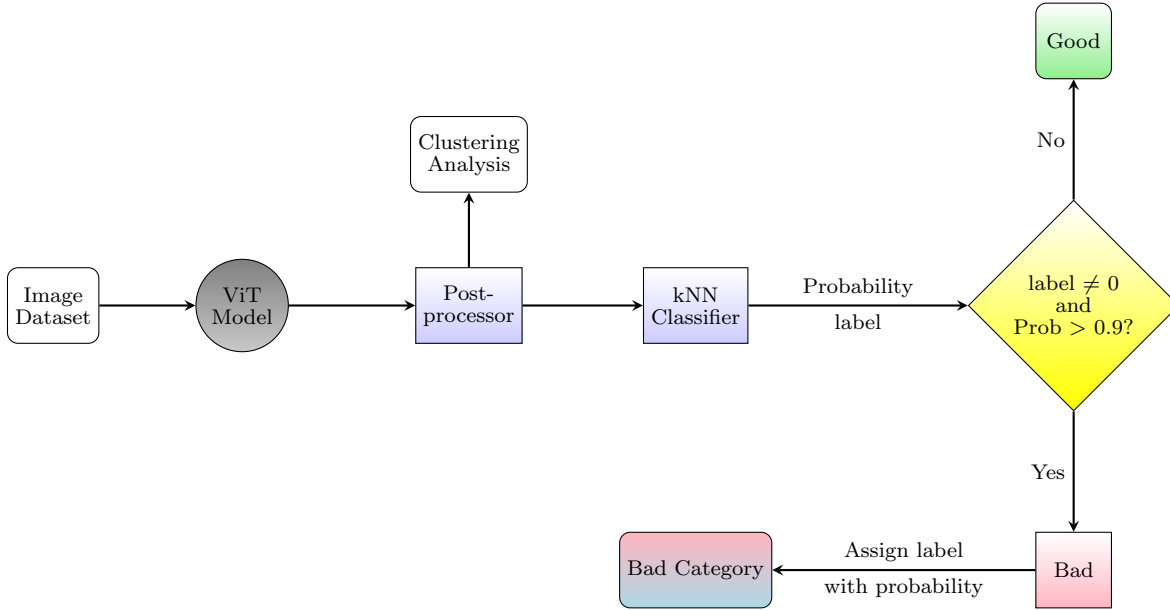


FIG. 4.— A depiction of how our pipeline identifies bad exposures.

3.1. Pipeline Overview

Our pipeline starts by feeding an image from the image dataset into the Deep Neural Network to generate an embedding with 768 dimensions (see Section 3.2). Some dimensions contain redundant or unstructured information (i.e., noise). We use post-processing to mitigate this noise to improve the overall prediction performance. The embedding post-processors include a scaler, a dimension reducer and a feature selector (Maharana et al. 2022). Output embeddings from the ViT are run through these post-processors before being passed to a kNN classifier (see Section 3.3). For the final step, the kNN classifier takes the post-processed embeddings and assigns a label with a probability based on the distance to the nearest neighbors in the training dataset. By comparing the probabilities and the labels, we can determine the qualities of the image from two perspectives: 1. *whether* the image is good or bad; 2. *if* the image is bad, which bad category it belongs to. Our end-to-end pipeline is illustrated in Figure 4.

3.2. The Vision Transformer

The Deep Neural Network we employ is a ViT (Dosovitskiy et al. 2021) trained on ImageNet (Deng et al. 2009) using the DINOv2 framework (Oquab et al. 2023). Specifically, the ViT model we use is the `vit_base` model with a register instance (Darcet et al. 2023), downloaded from PyTorch Hub, the specific model is

```
"facebookresearch/dinov2", "dinov2_vitb14_reg"
```

The `vit_base` model is an 18-block Vision Transformer with 768-dimensional embeddings and 12 attention heads. Similar to a conventional transformer model for Natural Language Processing (NLP), the ViT model is composed of a stack of transformer blocks. Each input image is divided into a grid of patches — 168x84 square patches each with 14x14 pixels in our chosen model — and then transformed into a sequence of vectors. Paddings with zeros are used to ensure the images are divisible by the patch size. This sequence of vectors is then fed into the transformer blocks to generate the embeddings. See Darcet et al. (2023), and references therein, for more details.

3.3. *k*-Nearest Neighbor Classifier

The *k*-Nearest Neighbor (kNN) classifier is a simple and effective algorithm for classification tasks based on the distance between the input data and the training data. We employ the `scikit-learn` implementation (Pedregosa et al. 2011) of the kNN classifier for its simplicity and efficiency. The labeled data provides the training set for the kNN classifier.

3.4. Training and Hyperparameter Optimization

Since we used a pretrained ViT model for the embedding generation, our focus in this paper is on training the downstream pipeline — the embedding post-processor and the kNN classifier. After the ViT model generates the embeddings for both the training and test datasets, we used the embeddings to *simultaneously* train the post-processor and the kNN classifier.

We employed the HPO technique (e.g., Franceschi et al. 2024) to search for the optimal hyperparameters for the post-processor and the kNN classifier. In particular, we defined ranges (for continuous variables) and options (for discrete variables) for hyperparameters and used the *Random Search with Successive Halving (RSSH)* algorithm (Jamieson & Talwalkar 2016; Li et al. 2018) to search for the optimal hyperparameters. The ranges and options are chosen to be

broad to let the *RSSH* algorithm explore for more globally optimal parameters. We also used 3-fold CV to evaluate the performance of the pipeline to ensure that our pipeline can be well generalized to a new dataset.

The core code components employed by our technique, and their associated optimal hyperparameters, are as follows. We used the *MinMaxScaler* to fix the range of each dimension in the embedding vector to $[0, 1]$. We used Principle Component Analysis (PCA) with 15 components to reduce embeddings’ dimensions from 384 to 15. We then further chose *VarianceThreshold* as our feature selector to remove insignificant (or “noisy”) features in the dimension-reduced embeddings with threshold=0.001. Finally, we found that the kNN classifier performed optimally using 7 neighbors and the “Manhattan distance” as the distance metric. The Manhattan distance⁹ (or L1 distance) is defined as:

$$d_{L1} = \sum_{i=0}^{dim} |p_i - q_i|$$

where p_i and q_i are the i -th dimension of the two embeddings p and q summed over dim dimensions. “Using 7 neighbors” in this sense means that the label and probability of each *test* image is determined by the distance to the 7 nearest neighbors in the *training* set.

3.5. Inference

After training and evaluation, we applied our pipeline to exposures that appear in DR11 of the LS (see Section 2) to infer which exposures might belong to the categories listed in Table 2. DR11 contains 283,633 exposures, so the inference step is somewhat computationally taxing. We therefore split the DR11 exposures into multiple batches and conducted the inference step in parallel on the National Energy Research Scientific Computing (NERSC) Center’s Perlmutter¹⁰ supercomputer using 2 nodes with 4 GPUs each. Fortunately, since the inference step doesn’t have to share gradients, it is embarrassingly parallelizable, and has very little communication overhead. Therefore, we can rapidly process many images in parallel with little-to-no performance degradation.

4. RESULTS

In this section, we present the performance of our trained pipeline on the DR10 data and inference results for the DR11 candidate exposures. We evaluate our results in two ways. First, a clustering analysis is performed to ensure images with similar features can be recognized by the model and separated in a cluster. We specifically select the *good* vs. *Ghost_Scatter* categories as a case study to illustrate how clusters are selected and interpreted by our pipeline.

Then, we evaluate our classification results using the multiclass *accuracy*, *precision*, *recall* and a more balanced accuracy referred to as the *F1 score* (Christen et al. 2023). In the equations below, the TP, TN, FP, and FN are the number of true positive, true negative, false positive, and false negative classifications, respectively. The multiclass accuracy is defined as (Grandini et al. 2020):

$$\text{Accuracy}_i = \frac{\text{TP}_i}{\text{the number of images with true label}_i} \quad (1)$$

The precision, recall and F1 scores are defined with respect to each class individually, so we follow the definition:

$$\text{Precision} = \frac{\text{TP}}{\text{TP} + \text{FP}} \quad (2)$$

$$\text{Recall} = \frac{\text{TP}}{\text{TP} + \text{FN}} \quad (3)$$

where, the F1 score is then defined as:

$$\text{F1} = 2 * \frac{\text{Precision} * \text{Recall}}{\text{Precision} + \text{Recall}} \quad (4)$$

We use the accuracy to measure the overall performance of the classifier, while we employ the F1 score to measure the balance between the *precision* and the *recall*.

The good exposures significantly outnumber the bad exposures, so the model has to capture imbalanced numbers across different categories. In this case, the raw *precision* of the model can better reflect the classification performance, as *precision* focuses on the classifications for the positive results (i.e., the categories to which the model actually assigns labels).

Beyond the results we will report in this section, it is worth noting that our pipeline is also very fast due to our parallelization across GPUs. For training, the ViT is already pre-trained and, our focus is on training the post-processor and the kNN classifier. The HPO process took a total of 2.5 hours to complete for our predefined set of parameters on a single node with a 128-core CPU. The only bottleneck in our pipeline is during the inference stage, when generating the embeddings using the ViT. Once the embeddings are generated, the kNN utilizes them without further intensive processing. To better optimize the embedding generation task, we distributed the inference tasks to 4 nodes, each with 4 GPUs. Overall, the inference step applied to all 5,672,660 LS DR11 images (283,633 exposures

⁹ <https://mathworld.wolfram.com/TaxicabMetric.html>

¹⁰ <https://docs.nersc.gov/systems/perlmutter/architecture>

with 20 CCD images drawn from each exposure, as described in Section 3) took a total of only 41 hours. On average, each GPU can process and generate embeddings for 8,647 images per hour.

4.1. Clustering Analysis

For a SSL algorithm, the performance is usually evaluated first by qualitatively checking how the embeddings are clustered to see if there are clear separations and structures among different potential characteristics of the images. A clear separation indicates that the model has definitively learned certain features of the images and is able to distinguish distinct patterns. This will ensure that the downstream task — the classification of new bad exposures — will have a good performance baseline (see Section 4.1.1 for more details).

We focus on using the training dataset to evaluate the clustering results, as it has known labels. The separation of the clusters is most easily visualized after running the embeddings through the dimension reduction process, the results of which are shown in Figure 5. Generally, well-separated and tightly-bound clusters indicate the model has learned enough features to distinguish different categories. We want to emphasize that plots such as Figure 5 – t-Distributed Stochastic Neighbor Embedding (t-SNE; van der Maaten & Hinton 2008) plots are only useful for qualitative analysis, and that the displayed clustering results have been collapsed over many dimensions. This means that the axes of the figures, and the coordinates of each single data point, are not intuitively *quantitatively* interpretable in and of themselves.

Figure 5 demonstrates that there is a clear clustering structure for the training dataset. There are several distinct areas that represent different categories of exposures. Most of the good exposures occupy the central parts of the space, while the bad exposures separate out across many different clusters. The good exposures typically contain various noticeable patterns that the model may pay attention to in a manner that a human visual inspector would not. Most prominently, emission from Galactic dust is easily identified by the model as a distinct feature. The model therefore incorrectly identifies dusty exposures as “bad”. We alleviate this issue for our final results by applying an extinction cut to the “good” exposure candidates to avoid dusty regions as described in Section 2.5.

The wide spread of the “good” exposures indicates that the corresponding features are very diverse and span an extensive range of the embedding space, as one would expect from a large imaging survey. For the “bad” exposures, the “ghost” exposures and the exposures in the “NObjects” category are spread out and overlap with the clusters of “good” exposures. It is worth remembering that Figure 5 displays a two dimensional reduction of the embeddings, so overlapping clusters might actually be quite distinct in higher dimensions. We compare the “good” and “ghost” exposures in the next sub-section to better characterize the separation of the clusters in higher dimensions and to illustrate the capability of the model to distinguish different features of the images.

For the other labels, the “bad” exposures are concentrated around certain parts of Figure 5 (i.e., they have low spread) and some of the categories separate well from the “good” exposures. A clear separation and a tight cluster indicate that the model has learned the features of the images well and should be able to distinguish patterns that correspond to different categories. These distinct patterns also provide a good basis for classifying test exposures as “good” or “bad,” as discussed in Section 4.2.

4.1.1. Case Study: Ghost_Scatter Exposures

We applied the Hierarchical Density-Based Spatial Clustering of Applications with Noise (HDBSCAN; Campello et al. 2015; McInnes et al. 2017) algorithm to a randomly-drawn sample of 10,000 CCD images from our whole dataset to study how our derived embeddings cluster (see Figure 6). We chose 10,000 images to reduce the computational cost for such a clustering analysis while keeping the sample size large enough to be statistically representative. HDBSCAN identified 70 clusters that included more than 10 data points. The distinctness of these clusters is a good indicator of how well individual exposures will be able to be separated into different categories. We also compare exposures via a 3D t-SNE plot in Figure 7, which provides additional information about the spatial distance and separations of clusters.

We focus on the *Ghost_Scatter* category as a case study to demonstrate what Figures 6 and 7 illustrate. The fact that the embeddings that correspond to the *Ghost_Scatter* category are almost entirely clustered in the top-right corners of Figures 6 and 7 demonstrates that the model has identified some unique features for these categories of exposures. HDBSCAN identified several clusters in this region, however, which is evidence that other CCD images share properties with exposures in the *Ghost_Scatter* category. To try to ascertain *which* types of images share properties with exposures in the *Ghost_Scatter* category, we selected two clusters based on the HDBSCAN clustering results for further analysis. The clusters are depicted in green and red in Figure 7. We randomly draw three example exposures from each of the two clusters, and present them in Figure 8. In this figure, we can observe that pupil ghosts exist in all of these exposures except for panel (a). A qualitative interpretation of the differences in the exposures is that the red *Ghost_Scatter* cluster from Figure 7 is more diffuse, and mixes with the good exposures, so the CCD images in exposures drawn from this cluster might be “slightly better” (more similar to a good exposure). On the other hand, exposures that lie in the green cluster in Figure 7 all show very clear, or even multiple, pupil ghosts.

4.2. Classification Performance

The general separation between clusters noted in Section 4.1 suggests that it is reasonable to proceed to classify exposures using our model. We therefore train and evaluate the kNN classifier discussed in Section 3.3 by applying it to the post-processed embeddings from samples described in Section 2. The classifier can predict the label with a

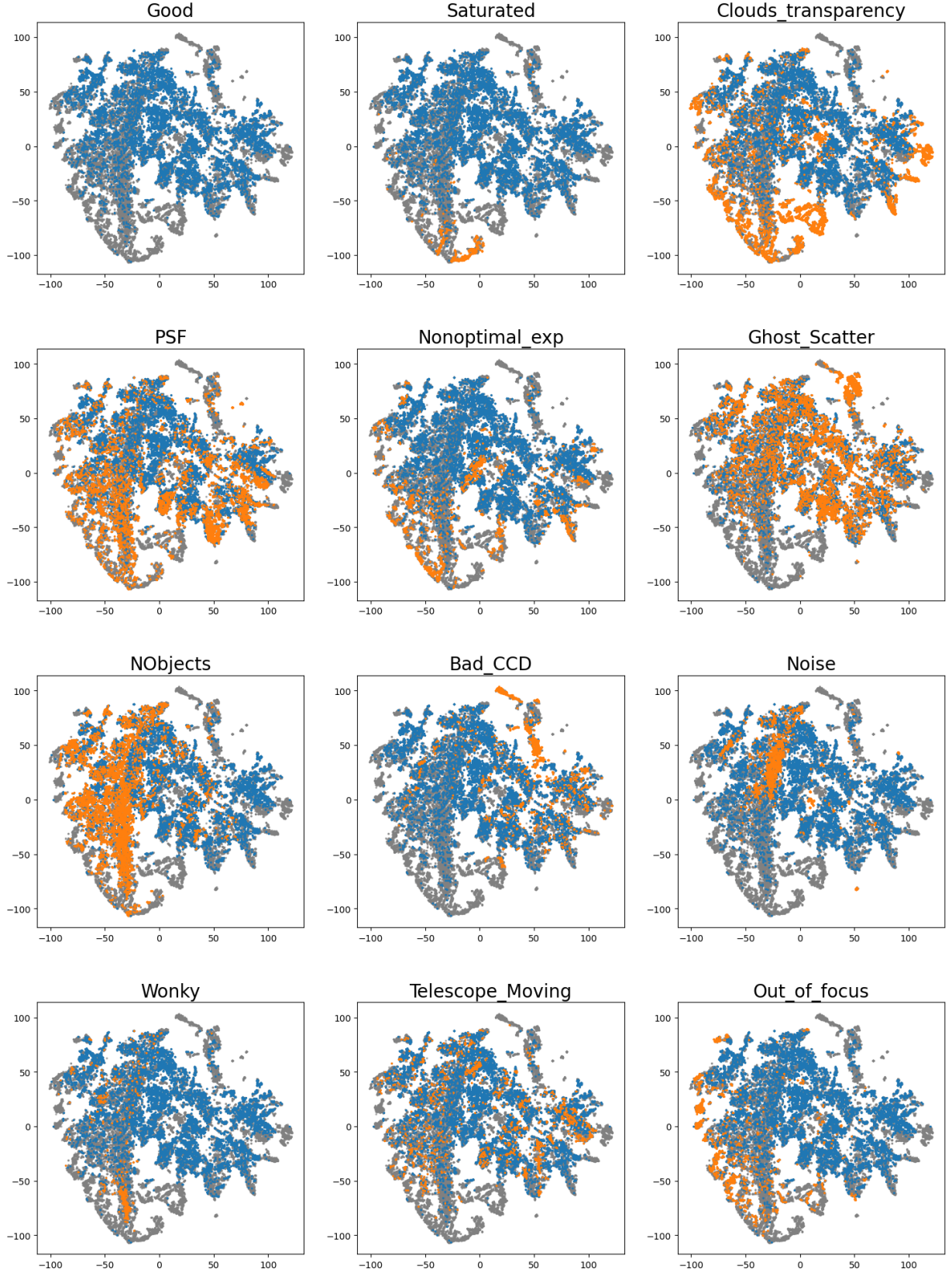


FIG. 5.— The clustering of the embeddings generated by the ViT model for the training dataset. The embeddings are processed through the same data processors described in Section 3.4, and they are further dimensionally reduced using the t-SNE method (van der Maaten & Hinton 2008) to help with visualization. The grey dots represent all training datasets, the blue dots depict “good” exposures, and the orange dots highlight the labeled exposures for each “bad” category. The top-left panel displays the good exposures, and the other panels show the bad exposures. The axes of the figures correspond to two dimensions of the t-SNE-reduced embeddings, and are not physically interpretable.

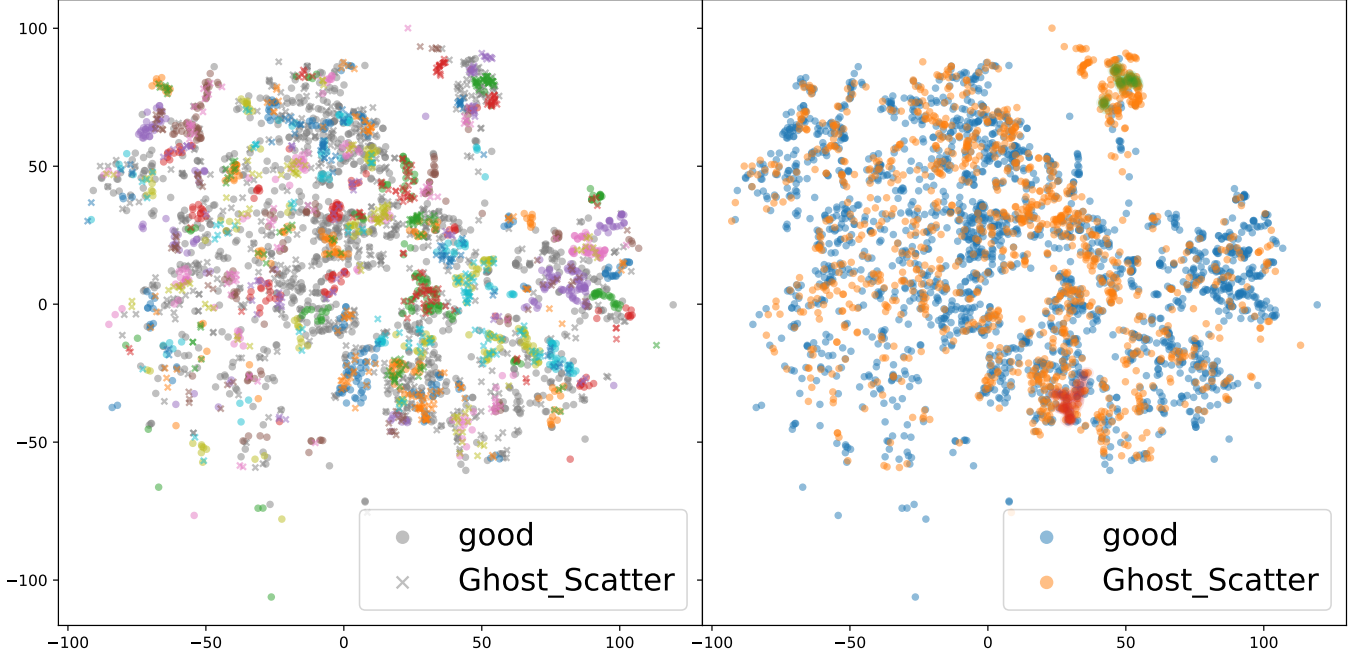


FIG. 6.— The left-hand panel depicts all clusters identified by the HDBSCAN clustering algorithm. The gray dots in the panel do not belong to any cluster. The right-hand panel highlights exposures in the *Ghost_Scatter* category and how they compare to “good” exposures. The red and green points displayed in this panel correspond to exposures displayed in Figure 8.

Category	Precision	Recall	F1-score	Support
<i>Good</i>	0.82	0.82	0.82	222
<i>Saturated</i>	0.98	0.97	0.98	122
<i>Cloud_transparency</i>	0.97	0.99	0.98	958
<i>PSF</i>	0.94	0.93	0.93	389
<i>Nonoptimal_exp</i>	0.94	0.96	0.95	204
<i>Ghost_Scatter</i>	0.92	0.80	0.85	222
<i>NObjects</i>	0.80	0.91	0.85	77
<i>Bad_CCD</i>	0.97	0.95	0.96	388
<i>Noise</i>	0.94	0.99	0.96	138
<i>Wonky</i>	0.71	1.00	0.83	12
<i>Telescope_Moving</i>	0.98	0.91	0.94	101
<i>Out_of_focus</i>	0.98	0.99	0.98	271

TABLE 3. THE CLASSIFICATION PERFORMANCE EVALUATED USING THREE SCORES. THE RIGHTMOST COLUMN (“SUPPORT”) RECORDS HOW MANY TEST IMAGES IN A GIVEN CATEGORY WERE USED IN THE CLASSIFICATION EVALUATION. THIS TABLE IS GENERATED FROM THE `CLASSIFICATION_REPORT` FUNCTION IN THE `SCIKIT-LEARN` PACKAGE.

probability associated with the distance to the nearest neighbors in the training dataset. We calculate this distance using the Manhattan distance metric, as described in Section 3.4. The number of nearest neighbors in this case is a hyperparameter, which is chosen to be 7 as it is the optimal parameter determined by the HPO process outlined in Section 3.4. For the multiclass classification, the probability of an image’s label in each category is calculated by the number of neighbors in the same category divided by the total number of neighbors:

$$P_{j=0\dots11} = \frac{N_{\text{neigh}=j}}{N_{\text{tot}}} = \frac{N_{\text{neigh}=j}}{7}$$

The numeric class labels are from 0 to 11 with 0 representing a good exposure and other labels representing each bad category.

After calculating the probability for each test exposure, we applied a probability cut of ≥ 0.9 to improve prediction accuracy for our classification results. Our final classification results are evaluated using accuracy, precision, recall and F1-score. The accuracy information is shown in Figure 9 as a confusion matrix. The precision, recall, and F1-score are shown in Table 3.

From the confusion matrix, our model achieves a high multiclass accuracy (see Equation 1) of higher than 0.8 for 9 out of our 11 categories of bad exposures. Table 3 shows that our model has a consistent classification performance across 11 categories. It is worth pointing out that *Wonky* has a limited number of images in the testing dataset, which can be non-representative, and thus will affect the classification result for this category. However, we expect exposures corresponding to the *Wonky* category to be generally rare in any case, as we usually know the precise category that a

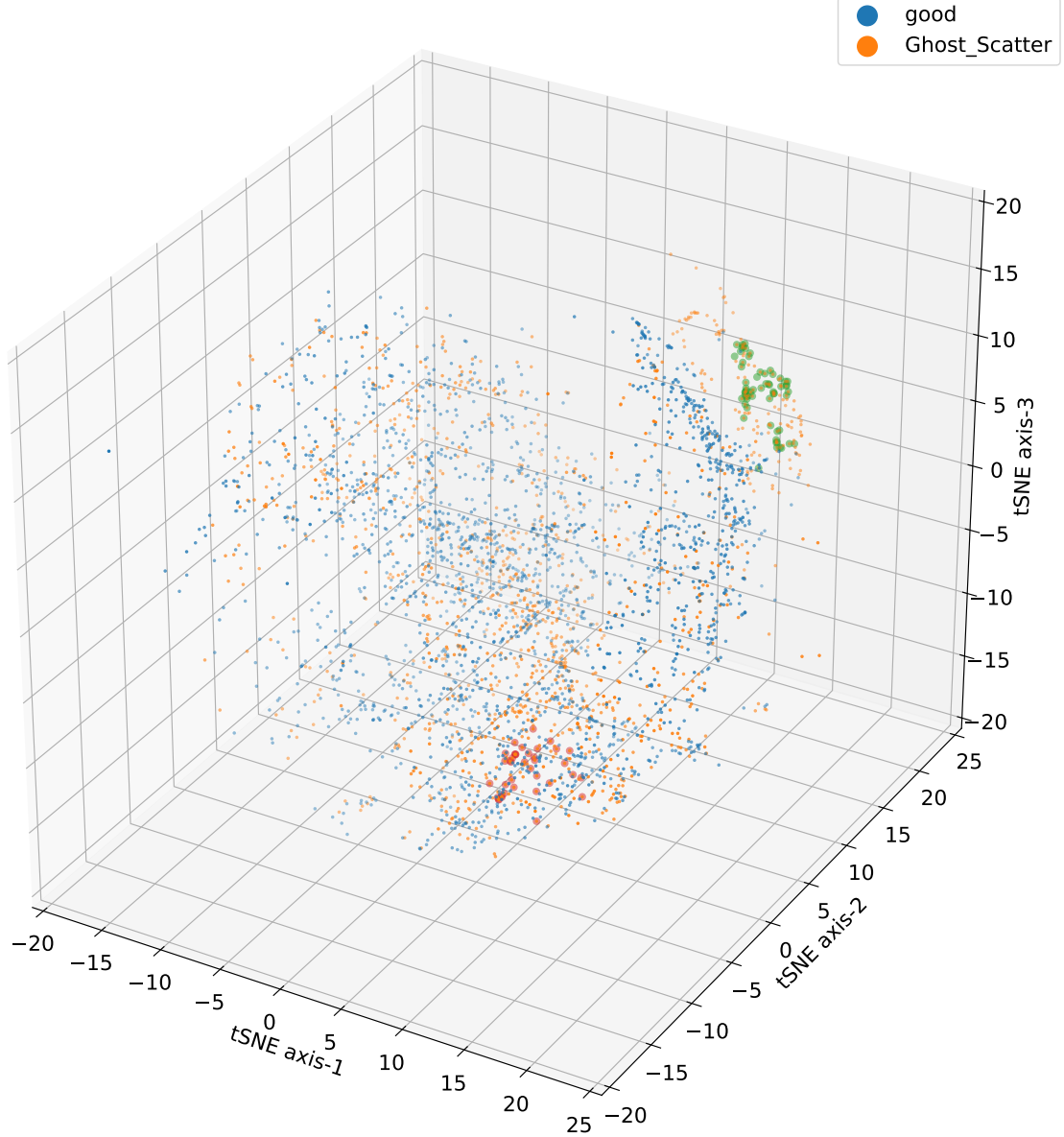


FIG. 7.— Three-dimensional t-SNE plot comparing exposures in the “good” and *Ghost_Scatter* categories with higher dimensionality than for Figure 5. The red and green points depicted in this figure correspond to exposures displayed in Figure 8. This plot can be viewed interactively at https://brookluo.github.io/projects/bad_exposure/, or by clicking on the figure.

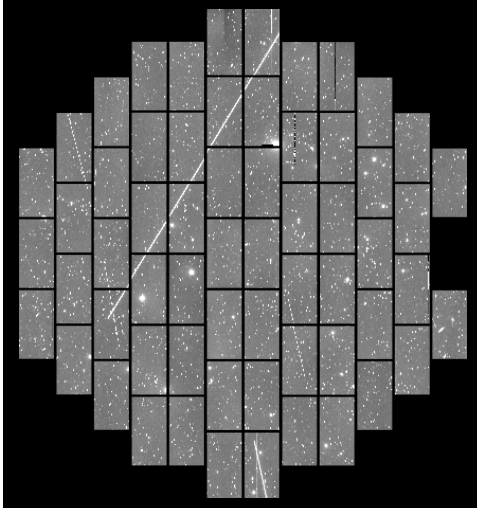
bad exposure belongs to.

The good performance demonstrated by our model across multiple evaluation metrics is due to several aspects of our approach. Fundamentally, we have confirmed in Section 4.1 that our model is able to recognize and distinguish different patterns. Furthermore, the 11 bad categories we use as labels are sufficiently representative to cover a wide range of photometric and technical issues. This may also imply that our model should be generalizable to other telescopes. Lastly, we applied a cut of > 0.9 in probability for our classification metrics, meaning we only focus on the most problematic exposures, which will inevitably improve the accuracy of our technique.

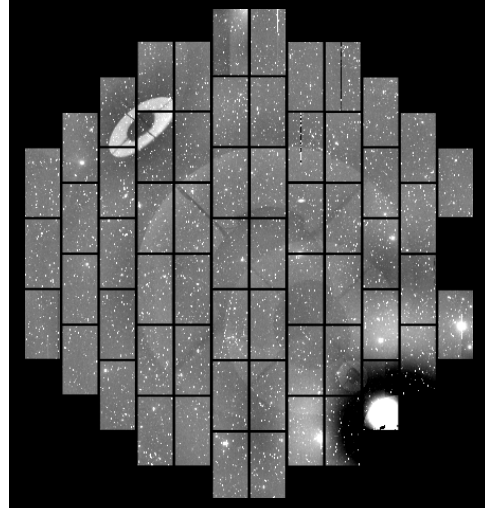
The two categories for which our model performed worst are the *Ghost_Scatter* and *Telescope_Moving* categories. The poor performance for *Ghost_Scatter* is likely due to ghost images spanning multiple CCDs, which we discuss more in Section 5.4. This is in contrast to most “bad” categories, which impact an entire exposure and so produce a pattern that is noticeable in every CCD image (regardless of which set of CCDs is randomly chosen by our census voting method discussed in Section 3). The low accuracy for the *Telescope_Moving* category is likely caused by this category having a relatively small training sample from which the classifier could learn.

4.3. Inference and Visual Inspection

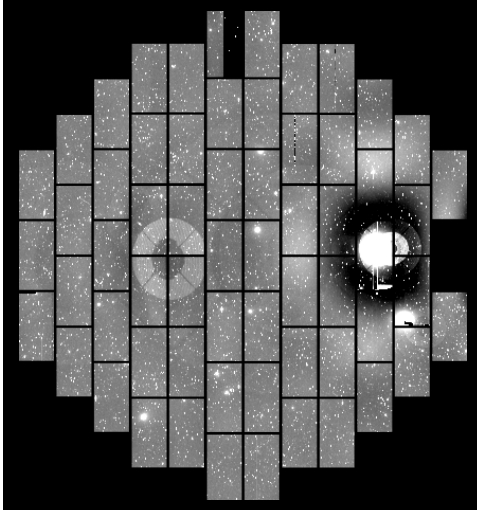
We ran our trained model on new exposures from the DECaLS and DELVE to determine which of these new exposures are consistent with being in a “bad” category, as detailed in Section 3.5. As derived in Section 4.2, we



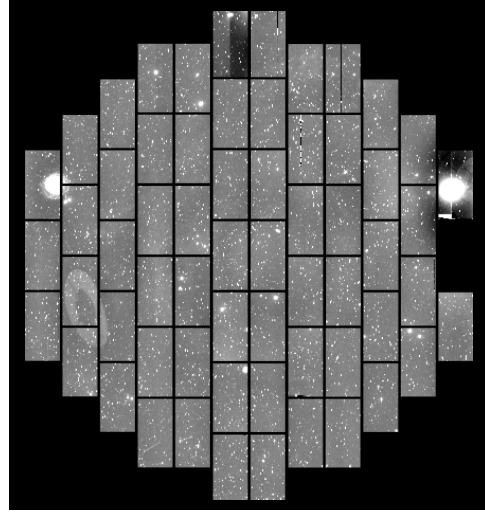
(a1) expnum=246861



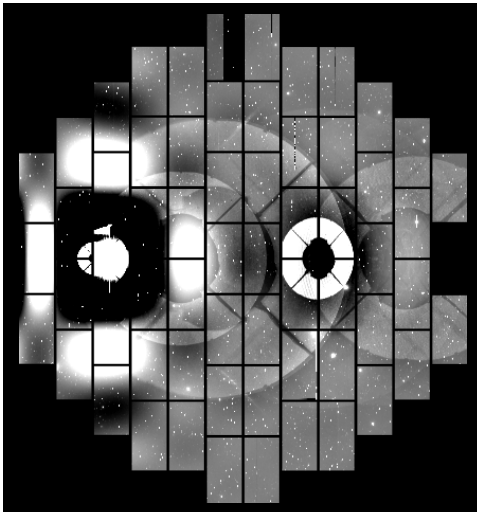
(b1) expnum=624625



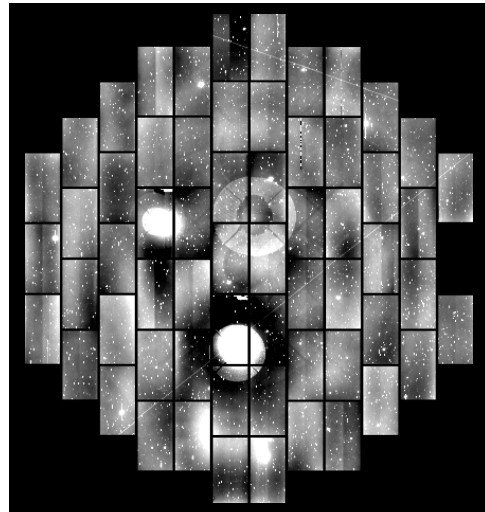
(a2) expnum=635208



(b2) expnum=730449



(a3) expnum=697269



(b3) expnum=862944

FIG. 8.— A set of sample exposures drawn from the two clusters depicted in Figure 7. The left-hand (right-hand) set of three panels show exposures that correspond to the red (green) cluster in Figure 7.

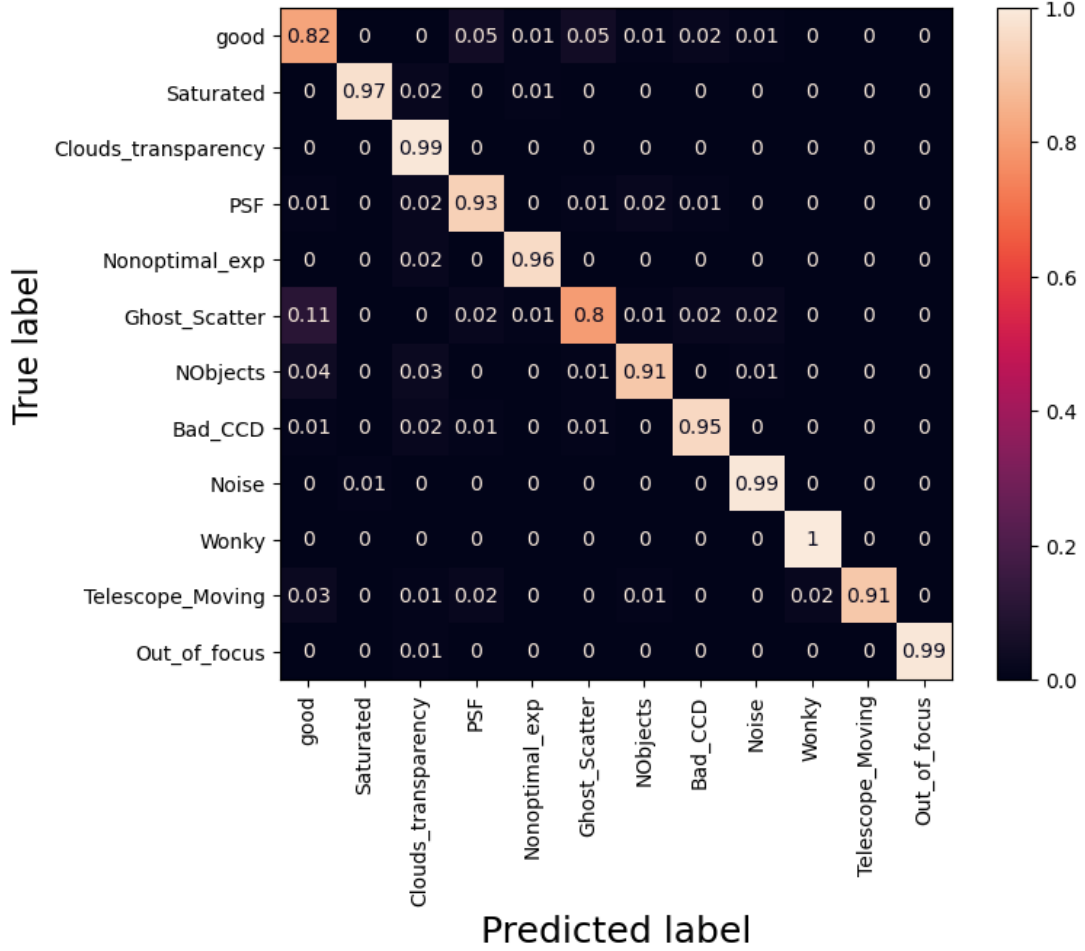


FIG. 9.— The confusion matrix for the multi-class classification problem. The displayed fractions correspond to the *multiclass accuracy* (see Equation 1).

applied a cut of ≥ 0.9 in probability to determine a “bad” exposure. This resulted in a sample of 4436 high-probability bad-exposure candidates.

Our ultimate goal is to identify new exposures to add to the *DECam Bad Exposure List* described in Section 2.1, with a view to augmenting that list for LS DR11. So, after running our identification pipeline, we visually inspected the bad exposure candidates with a view to only excluding extremely bad exposures. There are two reasons for this choice. First, because DECam has a wide field with 62 individual CCDs (or 61 CCDs as stated in Sec 1), many non-critical local issues can be identified by our pipeline as meaningful patterns. Second, because reaching a uniform depth is a major goal of the LS, it is preferable to err on the side of keeping marginal exposures.

Our visual inspection of the bad exposures was conducted by three experienced members of the LS collaboration. Each expert evaluated two aspects of each exposure — whether the exposure was indeed a bad exposure, and, if so, whether the category label assigned by the model was appropriate. The human experts’ responses were collated to form a final sample of 946 bad exposures. Some of these are existing exposures from LS DR9 and DR10 and some are identified only in new imaging assembled for DR11. All of the bad exposures will be rejected to produce the final reduced data for LS DR11.

5. DISCUSSION

In this section, we further analyze the results from our bad exposure identification pipeline. To do so, we consider two different sets of exposures: those used for the final LS DR9 and DR10 datasets, and new exposures identified from the DECaLS and DELVE campaigns intended to be used for LS DR11 (cf. Section 2). We will discuss how some exposures in the LS DR10 dataset are identified as “bad” by our pipeline but were entirely missed by the LS pipeline (henceforth **legacypipe**). Finally, we will also discuss the limitations of our current pipeline and some approaches that we might use to improve our current model and to adapt it to other imaging datasets.

5.1. Comparison between our pipeline and **legacypipe** for LS DR9 and DR10

The **legacypipe** is applied to data that has already been processed by the Community Pipeline (CP; Valdes et al. 2014, see also Section 2.4). The CP performs a number of initial data-reduction steps, including bias and dark-current

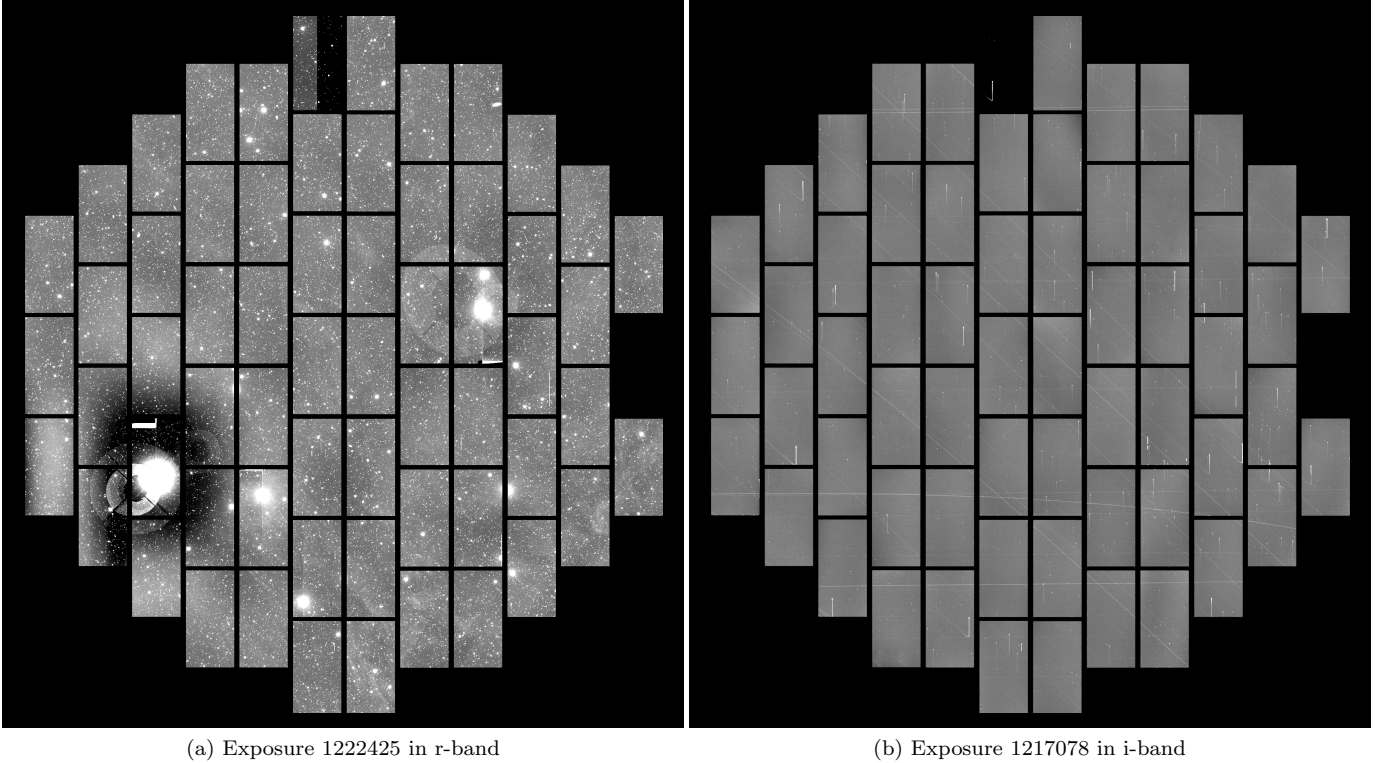


FIG. 10.— Two exposures in DR11 that are identified by our pipeline. The reason given by our ML for the exposure on the left is *Ghost_Scatter* and for the right one is *Telescope_Moving*. The classification result is verified and confirmed by human experts.

subtraction, flat-fielding and an initial background estimation. The **legacypipe** then processes each image to obtain photometry by performing full source and background modeling. A problematic exposure could be flagged by either the CP or by **legacypipe**. In addition, data reductions for DR9 and DR10 utilized a human-derived bad exposure list similar to that described in Section 2.1. However, some exposures we identified as outlined in Section 4.3 were not previously noticed by any of these LS reduction stages, and were included in LS DR9 or DR10. Our pipeline identified 2,591 candidates. Of these, only 579 exposures were also identified as bad by **legacypipe**. During our subsequent visual inspection, human experts verified 67 bad exposures that were included in DR9, and 92 bad exposures that were included in DR10. Our model therefore complements previous methods used by the LS to reject bad exposures.

Figure 11 shows an example of a bad exposure included in LS DR9 that would have been rejected by our pipeline. Our model classified this exposure as bad with label *PSF*, which typically means that an exposure includes stars with an irregular PSF. In actuality, this image does not have any noticeable PSF issues, but does contain prominent pupil ghosts. We expect that this incorrect label is due to the model’s limited focus on using single CCD images to capture each label (see the discussion in Section 5.4), and that ghosting across a single CCD could resemble a bad PSF.

5.2. New Bad Exposures

LS DR11 is expected to contain 107,940 new DECam exposures from the observing period 2020A – 2024A. We applied our pipeline to these exposures after they had been processed by the CP, and identified 1,732 bad exposure candidates, which is about 1.6% of the new exposures. The subsequent visual inspection confirmed 780 bad exposures. Running these exposures through the **legacypipe**, we find 708 mutually identified bad exposures and 72 exposures identified by our pipeline that are not flagged by **legacypipe**. We investigated these 72 exposures and discovered that they were mostly in the *Ghost_Scatter*, *NObjects*, and *Cloud_Transparency* categories.

The exposures identified by our pipeline will be included in the *DECam Bad Exposure List* (see Section 2.1) that the **legacypipe** will use to reject exposures from LS DR11.

5.3. The Benefits of DINO and SSL

Our approach to bad exposure identification takes advantage of recent advances in SSL by utilizing the pretrained DINO (v2) framework (Caron et al. 2021; Quab et al. 2023). Rather than training a self-supervised model from *scratch* on astronomical imaging alone, we extract rich embedding vectors from DINO to represent our telescope images. A major advantage of this strategy is that the DINO model, pretrained on ImageNet, has been exposed to a very diverse set of natural images, which allows the model to develop a more sophisticated understanding of image structure than would be possible through studying astronomical images alone. Leveraging a model that has already distilled information from millions of diverse images is also a computationally efficient way to add extra richness to our classification pipeline.

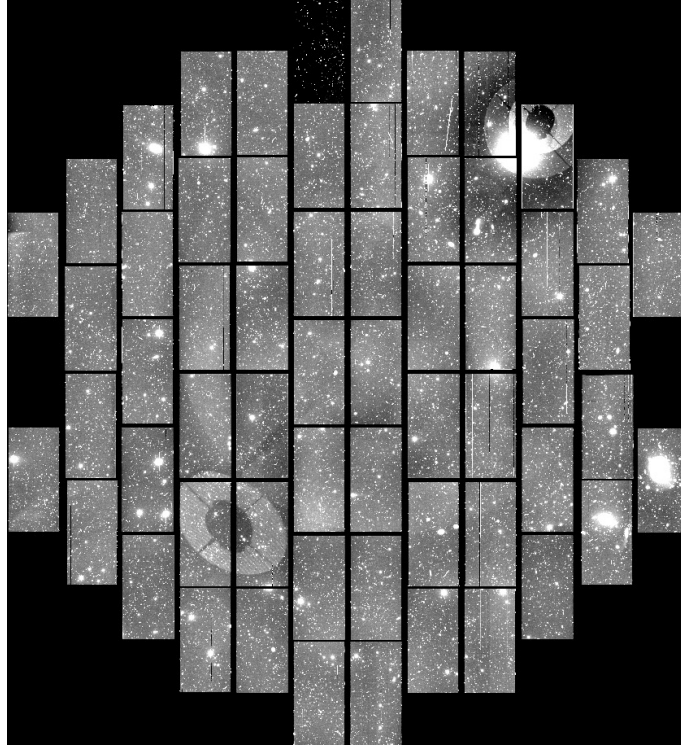


FIG. 11.— Exposure 260867 from the DECaLS (in the g band). The LS DR9 included this exposure, while our pipeline flagged this exposure as bad in the *Ghost_Scatter* category. Human experts later verified this exposure as bad during visual inspection. Several pupil ghosts are present in this exposure, which are likely caused by the bright star in the top-right corner.

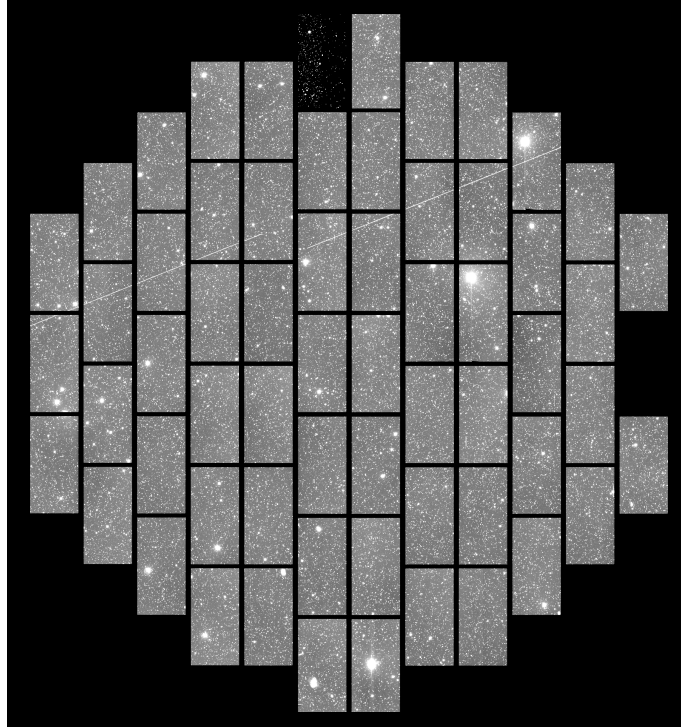


FIG. 12.— Exposure 1302430 (in the i -band). This is an example of an image that was misclassified as bad by our pipeline. Our pipeline classified this image as being in the *Telescope_Moving* category. However, human experts later evaluated this exposure as good during visual inspection. The misclassification is likely due to the two parallel and proximate satellite trails, which are a novel feature that might mimic movement of the telescope.

The self-supervised pretext tasks used in DINO’s training process also offer unique advantages over traditional supervised approaches (Albelwi 2022; Batutin 2024). While supervised learning methods are constrained by rigid label definitions, self-supervised pretext tasks (such as image augmentation recognition) enable the model to learn nuanced features that extend beyond simple classification boundaries and that otherwise might be overlooked.

Overall, in this work, we have found that using a framework like DINO in the context of SSL is practical, efficient, and returns excellent results when trying to classify bad exposures from large imaging surveys.

5.4. Limitations and Future Improvements

Although our current implementation can successfully identify bad exposures that are missed by other approaches, there are several ways in which our pipeline might be improved.

One potential failing of our methodology is that we treated the “good” exposures as merely being the complement of the “bad” exposures. Our rationale is that the good exposures do not have a generic set of patterns that can be used to identify them, and are thus difficult to describe, whereas the bad exposures have distinct features that can be categorized. However, a better approach might be to specifically classify both the bad and good exposures first, and then to further classify the bad exposures into subcategories. This could be achieved via a two-step classification process, with each step having an individual classifier.

Perhaps the critical drawback of our approach (cf. Section 2.6) is that our current technique focuses on information in a single CCD image and uses a census voting method based on drawing 20 randomly-chosen CCD images, to ascertain effects across a whole exposure. This is the natural approach to adopt because we individually process each CCD image. But, certain categories of bad exposures, such as the `Ghost.Scatter` category (see, e.g., Section 4.1.1), include patterns that span multiple CCDs. So, it is certainly possible that we misclassify some images as “good” that would clearly be considered “bad” based on coherent large-scale information. One concrete example is shown in Figure 12, which shows an exposure that our pipeline classified as bad in the `Telescope.Moving` category. However, this was subsequently flagged as a misclassification during visual inspection by human experts. In the exposure, there are two discontinuous, parallel satellite trails. This likely confused our model as it is a novel feature; most satellite trails in our exposures are continuous across an entire exposure. This, and similar, issues would likely be solved by a model that can analyze patterns that span multiple CCDs.

One way to better identify certain categories of bad exposure might therefore be to process the entire exposure at once. This would require more memory but, on the other hand, our current method is computationally expensive in processing each individual CCD. Another approach would be to process adjacent CCDs in bunches, by including additional positional encoding in the ViT. Perhaps ideally for our purposes, there are ML-based methods of *hierarchical* image learning for high-resolution images, such as the Hierarchical Image Pyramid Transformer (HIPT; Chen et al. 2022). HIPT potentially has the capability to process a whole exposure to discover large-scale patterns while simultaneously utilizing positional information to extract patterns on scales that correspond to one, or a few, CCDs.

Another issue is the current pipeline still requires human intervention to visually inspect the bad exposures identified by our model. Although this step is time-consuming, it is necessary to ensure that the bad exposures are indeed problematic, and to verify that the category assigned by our model is appropriate. This issue could be addressed if a general consensus could be reached on the definition of a bad exposure. With a larger set of bad exposures and a concrete standard for bad exposures, it might be possible to train a more sophisticated model that can classify bad exposures without any human intervention.

6. CONCLUSION

In this paper, we have introduced a new deep learning model to identify bad exposures in large imaging surveys. Our model is implemented based on a pre-trained vision transformer in the context of the DINO framework. We have explored the possibility of transferring information learned from a model trained on the ImageNet collection of general, feature-rich images to the classification of astronomical images from the LS. It is worth noting that this part of our work does not require any individual labels to infer patterns that correspond to different types of astronomical exposures.

We eventually classify our exposures based on metric distances in a high-dimensional space using a kNN approach. The training of the kNN *does* require a set of labeled bad exposures, for which we adopted a multi-class classification approach with 12 categories. We employed 11 categories for bad exposures, each describing a specific issue, and 1 category for good exposures. We compiled a bad exposure dataset using exposures flagged by human experts in LS and as part of the DELVE campaign. We treated exposures in LS DR9 that are not in the bad exposure dataset as generically *good*, and drew exposures from this set to form the “good” category.

We ran the pretrained ViT to generate embeddings that were later used to train the kNN classifier. The performance of our ViT+kNN pipeline was evaluated in two steps. We first evaluated the structure of the embeddings via clustering analysis to understand whether the model can successfully recognize and separate features that correspond to bad exposures. We then evaluated the classification performance of the kNN using several metrics, including accuracy and F1 score. Our model achieved a good and consistent performance with > 80% classification precision for most categories of bad exposures.

We applied our pipeline to identify bad exposures in preparation for DR11 of the LS. Our model identified 946 bad exposures in DR11. Of these, 159 bad exposures were already included in older exposures from DR9 and DR10 that will be reprocessed during DR11, and 786 bad exposures were identified in new exposures that will be processed for DR11. When comparing our bad exposure list with the list generated by the `legacypipe` software that is used to process

LS images, we found 708 mutual “bad” exposures and 72 bad exposures that were only identified by our pipeline. Our newly identified bad exposures will be included in the list of exposures that will be rejected by `legacypipe` when processing DR11 of the LS. These exposures are mostly in the *Ghost_Scatter* category, which indicates that these exposures contain pupil ghosts and/or scattered light.

With future large imaging survey telescopes, such as the Rubin Observatory (Ivezić et al. 2019), coming online, it will become increasingly impractical for human experts to identify bad exposures. Our model is consistent with a new approach; applying self-supervised learning to efficiently identify bad exposures in large imaging surveys with minimal human intervention. Moving forwards, new models and architectures, such as the Hierarchical Image Pyramid Transformer, may be of even more promise in both improving the classification accuracy for, and identifying various kinds of, bad exposures. Given the relative speed and scalability of our classification pipeline as described in Section 4, it should also be possible to identify bad exposures on-the-fly, with the potential to adjust observing strategies in real-time.

The approach we adopted in this work represents a novel intersection of transfer learning and self-supervised learning in astronomical image analysis. By leveraging the power of pretrained self-supervised models, our classification of bad exposures benefited from both the sophisticated feature-learning capabilities of SSL and the rich representational power acquired through training on diverse datasets. In some sense, our model’s ability to recognize patterns, textures, and structural anomalies transcends the domain gap between natural images and astronomical observations. In general, SSL may be a good choice for image classification in astronomy (and other domains) because it can provide a bridge between general computer vision and specialized scientific applications.

ACKNOWLEDGEMENTS

YL and ADM were supported by the U.S. Department of Energy, Office of Science, Office of High Energy Physics, under Award Number DE-SC0019022. YL was also partially supported by the University of Wyoming School of Computing Graduate Computing Scholarship and the Argonne National Laboratory W.J. Cody Associate Program. The work of AD and FV is supported by NOIRLab, which is managed by the Association of Universities for Research in Astronomy (AURA) under a cooperative agreement with the U.S. National Science Foundation.

The Legacy Surveys consist of three individual and complementary projects: the Dark Energy Camera Legacy Survey (DECaLS; Proposal ID #2014B-0404; PIs: David Schlegel and Arjun Dey), the Beijing-Arizona Sky Survey (BASS; NOAO Prop. ID #2015A-0801; PIs: Zhou Xu and Xiaohui Fan), and the Mayall z-band Legacy Survey (MzLS; Prop. ID #2016A-0453; PI: Arjun Dey). DECaLS, BASS and MzLS together include data obtained, respectively, at the Blanco telescope, Cerro Tololo Inter-American Observatory, NSF’s NOIRLab; the Bok telescope, Steward Observatory, University of Arizona; and the Mayall telescope, Kitt Peak National Observatory, NOIRLab. Pipeline processing and analyses of the data were supported by NOIRLab and the Lawrence Berkeley National Laboratory (LBNL). The Legacy Surveys project is honored to be permitted to conduct astronomical research on Iolkam Du’ag (Kitt Peak), a mountain with particular significance to the Tohono O’odham Nation. NOIRLab is operated by the Association of Universities for Research in Astronomy (AURA) under a cooperative agreement with the National Science Foundation. LBNL is managed by the Regents of the University of California under contract to the U.S. Department of Energy.

This project used data obtained with the Dark Energy Camera (DECam), which was constructed by the Dark Energy Survey (DES) collaboration. Funding for the DES Projects has been provided by the U.S. Department of Energy, the U.S. National Science Foundation, the Ministry of Science and Education of Spain, the Science and Technology Facilities Council of the United Kingdom, the Higher Education Funding Council for England, the National Center for Supercomputing Applications at the University of Illinois at Urbana-Champaign, the Kavli Institute of Cosmological Physics at the University of Chicago, Center for Cosmology and Astro-Particle Physics at the Ohio State University, the Mitchell Institute for Fundamental Physics and Astronomy at Texas A&M University, Financiadora de Estudos e Projetos, Fundacao Carlos Chagas Filho de Amparo, Financiadora de Estudos e Projetos, Fundacao Carlos Chagas Filho de Amparo a Pesquisa do Estado do Rio de Janeiro, Conselho Nacional de Desenvolvimento Cientifico e Tecnologico and the Ministerio da Ciencia, Tecnologia e Inovacao, the Deutsche Forschungsgemeinschaft and the Collaborating Institutions in the Dark Energy Survey. The Collaborating Institutions are Argonne National Laboratory, the University of California at Santa Cruz, the University of Cambridge, Centro de Investigaciones Energeticas, Medioambientales y Tecnologicas-Madrid, the University of Chicago, University College London, the DES-Brazil Consortium, the University of Edinburgh, the Eidgenossische Technische Hochschule (ETH) Zurich, Fermi National Accelerator Laboratory, the University of Illinois at Urbana-Champaign, the Institut de Ciencies de l’Espai (IEEC/CSIC), the Institut de Fisica d’Altes Energies, Lawrence Berkeley National Laboratory, the Ludwig Maximilians Universitat Munchen and the associated Excellence Cluster Universe, the University of Michigan, NSF’s NOIRLab, the University of Nottingham, the Ohio State University, the University of Pennsylvania, the University of Portsmouth, SLAC National Accelerator Laboratory, Stanford University, the University of Sussex, and Texas A&M University.

BASS is a key project of the Telescope Access Program (TAP), which has been funded by the National Astronomical Observatories of China, the Chinese Academy of Sciences (the Strategic Priority Research Program “The Emergence of Cosmological Structures” Grant # XDB09000000), and the Special Fund for Astronomy from the Ministry of Finance. The BASS is also supported by the External Cooperation Program of Chinese Academy of Sciences (Grant # 114A11KYSB20160057), and Chinese National Natural Science Foundation (Grant # 12120101003, # 11433005).

The Legacy Survey team makes use of data products from the Near-Earth Object Wide-field Infrared Survey Explorer (NEOWISE), which is a project of the Jet Propulsion Laboratory/California Institute of Technology. NEOWISE is funded by the National Aeronautics and Space Administration.

The Legacy Surveys imaging of the DESI footprint is supported by the Director, Office of Science, Office of High Energy Physics of the U.S. Department of Energy under Contract No. DE-AC02-05CH1123, by the National Energy Research Scientific Computing Center, a DOE Office of Science User Facility under the same contract; and by the U.S. National Science Foundation, Division of Astronomical Sciences under Contract No. AST-0950945 to NOAO.

APPENDIX

DATA AVAILABILITY STATEMENT

The DECaLS DR9 and DR10 data are available at <https://www.legacysurvey.org/>. The DR11 data is expected to be available later in 2025. The DECam bad exposure list, as compiled by LS for LS DR10.2, is available at https://github.com/legacysurvey/legacypipe/blob/DR10.2/py/legacyzpts/data/decam-bad_expid.txt. The DES and DELVE labeled bad exposures are available at <https://github.com/delve-survey/exclude>. All CP-reduced data for DECam are available from NOIRLab at <https://astroarchive.noirlab.edu/>.

REPRODUCIBILITY CONSIDERATIONS OF ML MODELS

We follow a number of best practices to make our result as reproducible as possible (see, e.g., Luo et al. 2023). For example, our source code and analysis notebooks are available in a public repository <https://github.com/Brookluo/ssl-bad-exposure-identification/releases/tag/v1.0>, and we have made sure to fix potentially changeable quantities, such as random seeds, software versions, and runtime environments. However, even following best practices to guard against irreproducibility, we recognize that our results may not be fully “bit-wise” reproducible. This is because the ML model we employ is mostly trained stochastically, so the results may vary slightly between different runs of our pipeline. But, we expect any subsequent results to be *consistent* with the reported results in this paper provided the pretrained ViT model remains unchanged on PyTorch Hub.

REFERENCES

- Albelwi, S. 2022, *Entropy*, 24, 551, doi: [10.3390/e24040551](https://doi.org/10.3390/e24040551)
- Astropy Collaboration, Price-Whelan, A. M., Lim, P. L., et al. 2022, *ApJ*, 935, 167, doi: [10.3847/1538-4357/ac7c74](https://doi.org/10.3847/1538-4357/ac7c74)
- Azad, R., Kazerouni, A., Heidari, M., et al. 2024, *Medical Image Analysis*, 91, 103000, doi: <https://doi.org/10.1016/j.media.2023.103000>
- Balestrieri, R., Ibrahim, M., Sobal, V., et al. 2023, *A Cookbook of Self-Supervised Learning*, arXiv, doi: [10.48550/ARXIV.2304.12210](https://arxiv.org/abs/2304.12210)
- Batutin, A. 2024, *Self-Supervised Learning Harnesses the Power of Unlabeled Data*. <https://shelf.io/blog/self-supervised-learning-harnesses-the-power-of-unlabeled-data>
- Campello, R. J. G. B., Moulavi, D., Zimek, A., & Sander, J. 2015, *ACM Trans. Knowl. Discov. Data*, 10, doi: [10.1145/2733381](https://doi.org/10.1145/2733381)
- Caron, M., Touvron, H., Misra, I., et al. 2021, in *Proceedings of the International Conference on Computer Vision (ICCV)*
- Chang, C., Drlica-Wagner, A., Kent, S., et al. 2021, *Astronomy and Computing*, 36, 100474, doi: [10.1016/j.ascom.2021.100474](https://doi.org/10.1016/j.ascom.2021.100474)
- Chen, R. J., Chen, C., Li, Y., et al. 2022, *Scaling Vision Transformers to Gigapixel Images via Hierarchical Self-Supervised Learning*. <https://arxiv.org/abs/2206.02647>
- Christen, P., Hand, D. J., & Kirielle, N. 2023, *ACM Comput. Surv.*, 56, doi: [10.1145/3606367](https://doi.org/10.1145/3606367)
- Darcet, T., Oquab, M., Mairal, J., & Bojanowski, P. 2023, *Vision Transformers Need Registers*
- Deng, J., Dong, W., Socher, R., et al. 2009, in *2009 IEEE Conference on Computer Vision and Pattern Recognition*, 248–255, doi: [10.1109/CVPR.2009.5206848](https://doi.org/10.1109/CVPR.2009.5206848)
- DES Collaboration. 2016, *Monthly Notices of the Royal Astronomical Society*, 460, 1270, doi: [10.1093/mnras/stw641](https://doi.org/10.1093/mnras/stw641)
- DESI Collaboration, Aghamousa, A., Aguilar, J., et al. 2016, *arXiv e-prints*, arXiv:1611.00036, doi: [10.48550/arXiv.1611.00036](https://arxiv.org/abs/1611.00036)
- Dey, A., Schlegel, D. J., Lang, D., et al. 2019, *AJ*, 157, 168, doi: [10.3847/1538-3881/ab089d](https://doi.org/10.3847/1538-3881/ab089d)
- Dosovitskiy, A., Beyer, L., Kolesnikov, A., et al. 2021, in *International Conference on Learning Representations*. <https://openreview.net/forum?id=YicbFdNTTy>
- Drlica-Wagner, A., Carlin, J. L., Nidever, D. L., et al. 2021, *ApJS*, 256, 2, doi: [10.3847/1538-4365/ac079d](https://doi.org/10.3847/1538-4365/ac079d)
- Drlica-Wagner, A., Ferguson, P. S., Adamów, M., et al. 2022, *ApJS*, 261, 38, doi: [10.3847/1538-4365/ac78eb](https://doi.org/10.3847/1538-4365/ac78eb)
- Flaugher, B., Diehl, H. T., Honscheid, K., et al. 2015, *AJ*, 150, 150, doi: [10.1088/0004-6256/150/5/150](https://doi.org/10.1088/0004-6256/150/5/150)
- Franceschi, L., Donini, M., Perrone, V., et al. 2024, *Hyperparameter Optimization in Machine Learning*, arXiv, doi: [10.48550/ARXIV.2410.22854](https://arxiv.org/abs/2410.22854)
- Grandini, M., Bagli, E., & Visani, G. 2020, *Metrics for Multi-Class Classification: an Overview*. <https://arxiv.org/abs/2008.05756>
- Gui, J., Chen, T., Zhang, J., et al. 2024, *A Survey on Self-supervised Learning: Algorithms, Applications, and Future Trends*. <https://arxiv.org/abs/2301.05712>
- Ivezić, Ž., Kahn, S. M., Tyson, J. A., et al. 2019, *The Astrophysical Journal*, 873, 111, doi: [10.3847/1538-4357/ab042c](https://doi.org/10.3847/1538-4357/ab042c)
- Jamieson, K., & Talwalkar, A. 2016, in *Proceedings of Machine Learning Research*, Vol. 51, *Proceedings of the 19th International Conference on Artificial Intelligence and Statistics*, ed. A. Gretton & C. C. Robert (Cadiz, Spain: PMLR), 240–248. <https://proceedings.mlr.press/v51/jamieson16.html>
- Kent, S. M. 2013, *Ghost Images in DECam [Slides]*, Tech. rep., Fermi National Accelerator Lab. (FNAL), Batavia, IL (United States), doi: [10.2172/1690257](https://doi.org/10.2172/1690257)
- Kirillov, A., Mintun, E., Ravi, N., et al. 2023, *Segment Anything*. <https://arxiv.org/abs/2304.02643>
- Lang, D., Hogg, D. W., Jester, S., & Rix, H.-W. 2009, *The Astronomical Journal*, 137, 4400–4411, doi: [10.1088/0004-6256/137/5/4400](https://doi.org/10.1088/0004-6256/137/5/4400)
- Lang, D., Hogg, D. W., & Mykytyn, D. 2016, *The Tractor: Probabilistic astronomical source detection and measurement*, *Astrophysics Source Code Library*, record ascl:1604.008
- Li, L., Jamieson, K., DeSalvo, G., Rostamizadeh, A., & Talwalkar, A. 2018, *Hyperband: A Novel Bandit-Based Approach to Hyperparameter Optimization*. <https://arxiv.org/abs/1603.06560>
- Luo, Y., Zhang, Q., Haas, R., Etienne, Z. B., & Allen, G. 2023, *Classical and Quantum Gravity*, 41, 025002, doi: [10.1088/1361-6382/ad13c5](https://doi.org/10.1088/1361-6382/ad13c5)
- Maharana, K., Mondal, S., & Nemade, B. 2022, *Global Transitions Proceedings*, 3, 91, doi: [10.1016/j.gltp.2022.04.020](https://doi.org/10.1016/j.gltp.2022.04.020)
- McInnes, L., Healy, J., & Astels, S. 2017, *Journal of Open Source Software*, 2, 205, doi: [10.21105/joss.00205](https://doi.org/10.21105/joss.00205)
- Morgan, E., Gruendl, R. A., Menanteau, F., et al. 2018, *Publications of the Astronomical Society of the Pacific*, 130, 074501, doi: [10.1088/1538-3873/aab4ef](https://doi.org/10.1088/1538-3873/aab4ef)
- Myers, A. D., Moustakas, J., Bailey, S., et al. 2023, *The Astronomical Journal*, 165, 50, doi: [10.3847/1538-3881/aca5f9](https://doi.org/10.3847/1538-3881/aca5f9)

- National Academies of Sciences, Engineering, and Medicine. 2023, Pathways to Discovery in Astronomy and Astrophysics for the 2020s (Washington, DC: The National Academies Press), doi: [10.17226/26141](https://doi.org/10.17226/26141)
- Oquab, M., Darcet, T., Moutakanni, T., et al. 2023, DINOv2: Learning Robust Visual Features without Supervision, arXiv. <http://arxiv.org/abs/2304.07193>
- Parisot, O., Bruneau, P., & Hitzelberger, P. 2023, in Proceedings of the 12th International Conference on Data Science, Technology and Applications - DATA, INSTICC (SciTePress), 279–286, doi: [10.5220/0012073800003541](https://doi.org/10.5220/0012073800003541)
- Patterson, B. A., & Wells, M. 2003, in Specialized Optical Developments in Astronomy, ed. E. Atad-Ettinger & S. D’Odorico, Vol. 4842, International Society for Optics and Photonics (SPIE), 116 – 127, doi: [10.1117/12.459469](https://doi.org/10.1117/12.459469)
- Pedregosa, F., Varoquaux, G., Gramfort, A., et al. 2011, Journal of Machine Learning Research, 12, 2825
- Rolnick, D., Veit, A., Belongie, S., & Shavit, N. 2018, Deep Learning is Robust to Massive Label Noise. <https://arxiv.org/abs/1705.10694>
- Schlegel, D. J., Finkbeiner, D. P., & Davis, M. 1998, ApJ, 500, 525, doi: [10.1086/305772](https://doi.org/10.1086/305772)
- Steinkraus, D., Buck, I., & Simard, P. 2005, in Eighth International Conference on Document Analysis and Recognition (ICDAR’05), 1115–1120 Vol. 2, doi: [10.1109/ICDAR.2005.251](https://doi.org/10.1109/ICDAR.2005.251)
- Stone, M. 1974, Journal of the Royal Statistical Society Series B: Statistical Methodology, 36, 111–133, doi: [10.1111/j.2517-6161.1974.tb00994.x](https://doi.org/10.1111/j.2517-6161.1974.tb00994.x)
- Stubbs, C. W., & Tonry, J. L. 2006, The Astrophysical Journal, 646, 1436–1444, doi: [10.1086/505138](https://doi.org/10.1086/505138)
- Tan, C. Y., Cerny, W., Drlica-Wagner, A., et al. 2025, The Astrophysical Journal, 979, 176, doi: [10.3847/1538-4357/ad9b0c](https://doi.org/10.3847/1538-4357/ad9b0c)
- Tanoglidis, D., Čiprijanović, A., Drlica-Wagner, A., et al. 2021, DeepGhostBusters: Using Mask R-CNN to Detect and Mask Ghosting and Scattered-Light Artifacts from Optical Survey Images. <https://arxiv.org/abs/2109.08246>
- Valdes, F., Gruendl, R., & DES Project. 2014, in Astronomical Society of the Pacific Conference Series, Vol. 485, Astronomical Society of the Pacific Conference Series, ed. N. Manset & P. Forshay, 379
- van der Maaten, L., & Hinton, G. 2008, Journal of Machine Learning Research, 9, 2579
- van Dokkum, P. G. 2001, Publications of the Astronomical Society of the Pacific, 113, 1420, doi: [10.1086/323894](https://doi.org/10.1086/323894)
- Vaswani, A., Shazeer, N., Parmar, N., et al. 2017, in Advances in Neural Information Processing Systems, ed. I. Guyon, U. V. Luxburg, S. Bengio, H. Wallach, R. Fergus, S. Vishwanathan, & R. Garnett, Vol. 30 (Curran Associates, Inc.). https://proceedings.neurips.cc/paper_files/paper/2017/file/3f5ee243547dee91fbd053c1c4a845aa-Paper.pdf
- Zhang, K., & Bloom, J. S. 2020, The Astrophysical Journal, 889, 24, doi: [10.3847/1538-4357/ab3fa6](https://doi.org/10.3847/1538-4357/ab3fa6)
- Zou, H., Zhou, X., Fan, X., et al. 2017, PASP, 129, 064101, doi: [10.1088/1538-3873/aa65ba](https://doi.org/10.1088/1538-3873/aa65ba)

This paper was built using the Open Journal of Astrophysics L^AT_EX template. The OJA is a journal which provides fast and easy peer review for new papers in the **astro-ph** section of the arXiv, making the reviewing process simpler for authors and referees alike. Learn more at <http://astro.theoj.org>.